August 2014

Cryoimaging-Microscopy Implementation for 3D Optical Imaging

Mohammad MasoudiMotlagh
University of Wisconsin-Milwaukee

CRYOIMAGING-MICROSCOPY IMPLEMENTATION FOR 3D OPTICAL IMAGING

by

Mohammad MasoudiMotlagh

A Thesis Submitted in

Partial Fulfillment of the

Requirements for the Degree of

Master of Science

in Engineering

at

The University of Wisconsin-Milwaukee

August 2014

ABSTRACT

CRYOIMAGING-MICROSCOPY IMPLEMENTATION FOR 3D OPTICAL IMAGING

by

Mohammad MasoudiMotlagh

The University of Wisconsin-Milwaukee, 2014
Under the Supervision of Professor Mahsa Ranji

The structures and biochemistry properties of biological tissues are mostly affected by diseases. The visualization of organ structure and biochemistry helps in early detection and progression monitoring of diseases.

Although, 2D imaging has traditionally been used to gain information from the tissue, it does not accurately represent many of the structures and functions. There currently exists a need for sensitive and specific methods to show detailed information about the structure of the tissue with high resolution and in 3D. The potential advantage of the high resolution 3D images is the ability to accurately probe structural and biochemical properties of the tissue.

Not only the changes in structure, but also the changes in temporal physiological responses affected by oxidative stress (OS) at cellular levels. Thus, it would be valuable to detect the cellular metabolic states, which play a key role in understanding the pathogenesis of the disease, and to develop instruments to detect high resolution 3D images of the tissue.

The objective of this research is to develop a second generation fluorescence optical imaging instrument to image the cellular redox state in 3D, in control and diseases conditions.

I have improved upon one of optical instrument, called cryoimager software and hardware wise to enable higher resolution images. This higher resolution imaging resembles the microscopy capability in cryo temperatures for high resolution 3D imaging.

In conclusion, high resolution optical instrumentation combined with signal and image processing tools provide quantitative physiological and structural information of diseased tissue.

TABLE OF CONTENTS

LIST OF FIGURES

LIST OF TABLES

LIST OF ABBREVIATIONS

ADP - Adenosine Diphosphate

ATP - Adenosine Triphosphate

BCL-2 - B Cell Lymphoma Gene

BPD - Bronchopulmonary Dysplasia

CCD - Charge-Coupled Device

CT - Computerized Tomography

Eng - Endoglin

$FADH_2$ - Flavin Adenine Dinucleotide

FOV - Field Of View

HHT-1 - Hereditary Hemorrhagic Telangiectasia

LN2 - Liquid Nitrogen

LP/mm - Line Per millimeter

NADH - Nicotinamide Adenine Dinucleotide

NADPH - Nicotinamide Adenine Dinucleotide Phosphate

NAD(P)H - Combination of NADH and NADPH

ND - Neutral Density

OS - Oxidative Stress

ROS - Reactive Oxygen Species

ACKNOWLEDGMENTS

I take this opportunity to express my deep sense of gratitude to my graduate advisor, Dr. Mahsa Ranji, for her continuous encouragement, guidance and support during this research. In addition, I am grateful to Dr. Ramin Pashaie whose enlightening ideas and experiences were highly valuable during the completion of my Master program.

This work would not have been possible without the help of a few collaborators. I would like to thank Dr. Sheibani and Dr. Sorenson from University of Wisconsin Madison, who have provided me with the tissue samples studied in this research.

I also would like to thank my parents for being so supportive of me throughout my life, both academically and personally. I want to thank my brothers who have been my friends over the years. I appreciate the support of Dr. Alireza Shapoury during my academic pursuit as well.

Last, but not least, I want to thank all my friends at Biophotonics Lab, especially Zahra Ghanian, Whitney Linz and Reyhaneh Sepehr who helped me a lot to finish this thesis.

Chapter 1

Introduction and Background

1 Introduction and Background

One of the fastest growing research areas in bioengineering is biophotonics. As the name implies, biophotonics is the study of the interaction between light and biological tissue [2]. This interaction can be studied in two different categories. One is the properties of the tissue and the other is the changes that light can induce in a biological sample after the interaction. A majority of the current research in the biophotonics field is about the properties of the tissue and thus tissue disease diagnosis.

I develop cryo-microscopy imaging technique to monitor the structures of the tissue with diseases such as cardiopulmonary injuries and diabetes as well as the metabolic state of the tissue.

1.1 My Contributions

In this research, my goal was to increase resolution of cryoimaging to visualize the structural changes in 3D due to the diseases, and correlate the results with the metabolic changes in the tissue. To reach the aforementioned plan, I contributed to implementation of the microscopy capability of a device named cryoimager. The cryoimager is an automatic image acquisition instrument that sequentially slices the frozen tissue and acquires fluorescent images of each slice. The fluorescent images then are analyzed and the metabolic changes of the tissue are quantified. The physiological marker to show the changes in the metabolism is mitochondrial redox ratio of the tissue.

The implementation includes the study and design of the new cryo-microscopy setup by choosing, ordering and assembling the appropriate equipment and linking them to the software I implemented, based on the limitations and challenges existed. Three main limitations which I overcame are taking magnified images by still holding high resolution images properties, eliminating the chromatic aberration of the imaging lens and compensating the limited field of view in highly magnified images. Picking an appropriate lens based on our application, moving the position of the lens by using a linear translation micro-stage and raster scanning are the solutions I figured out to the aforementioned challenges. The new cryo-microscopy setup completed by solving problems such as non-homogeneity illumination, implementing a stitching software for a convenient and rapid post-imaging processing and ultimately result validation by testing the system on many scrap samples.

In my research, I studied the mitochondrial redox ratio in bronchopulmonary-dysplasia (BPD) injury models in mice lungs. Bronchopulmonary dysplasia is a chronic lung condition that affects premature infants who receive supplemental oxygen (hyperoxia) or ventilator support for long periods of time. The results of this study validated the performance of the cryoimaging technique in measuring the oxidative state of the tissues. I also studied the structural changes in the tissue due to disease which affects the mitochondrial redox state of the tissue with the new cryo-microscopy setup. A dominant vascular dysplasia (HHT-1 or Endoglin+/-) injury model was studied to reach this goal. HHT-1 (Hereditary hemorrhagic telangiectasia) is a good model of a disease in which the vasculature network of different organs is affected. This disease is caused by

loss-of-function mutations in the human Endoglin gene and results in excessive bleeding and vascular malformation due to failure to recruit perivascular supporting cells to the newly forming blood vessels [51]. HHT-1 causes frequent nose bleeds, telangiectases, mucosa, and arteriovenous malformations in lung, liver, kidney, and brain [51] [52].

1.2 Biology Background

1.2.1 Cell Structure and the Mitochondrion

All biological organisms are made up of cells [3] and one of the most important factors in any biological system is cellular and sub-cellular homeostasis.

Homeostasis is a state in which everything within the cell is in equilibrium and functioning properly. If the cell is not homeostasis, it is not healthy and will results in cell death. Injuries and diseases within the tissue cause irregularities in the cell function.

Although, there are many cellular organelles responsible for organism health, mitochondrion plays the most important role. Mitochondria are often referred to as the power plants of the cell since energy production takes place in them.

The mitochondrion is responsible for many cellular functions, including metabolic processes [4], which are the chemical reactions necessary for sustaining life in a biological organism [5]. A cell structure including the mitochondria is shown in Figure 1.1 [6].

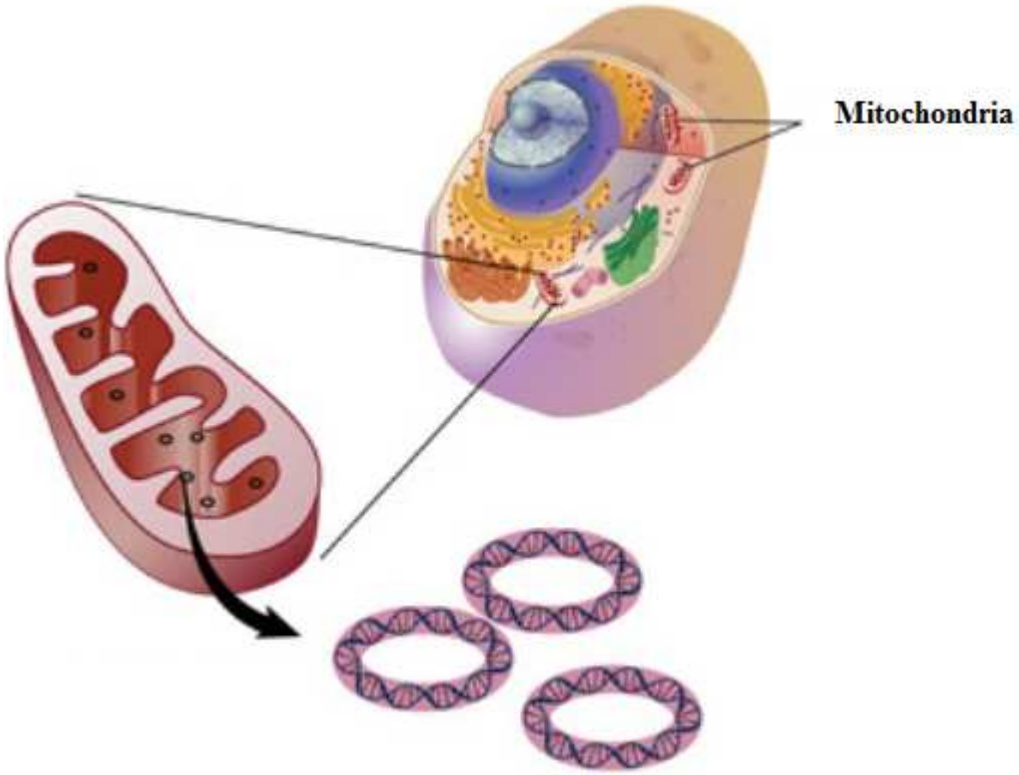

Figure 1.1: Cell structure including the mitochondria [6].

A form of cellular respiration that requires oxygen to generate energy is called aerobic respiration. In this process, coenzymes present in the mitochondria are oxidized and produce energy usable by cells [5] [7] [8]. Therefore, the amount of energy that supplied to the cell is highly dependent on the amount of oxygen present in the mitochondria. The energy is termed ATP and the majority of the energy is produced through electron transport chain. Electron transport chain is the cellular mechanisms used for extracting energy from redox reactions such as respiration [9]. A diagram of mitochondrial electron transport chain is shown in Figure 1.2 [10].

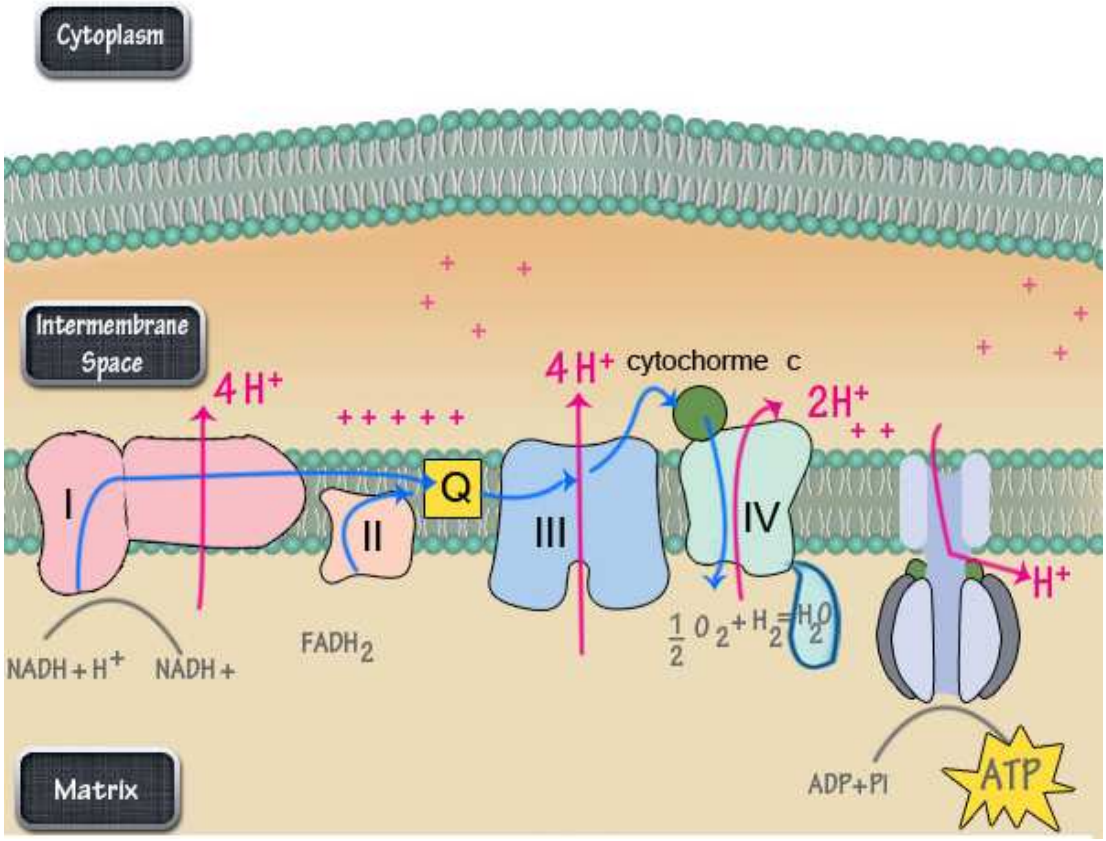

Figure 1.2: Electron transport chain diagram [10].

The electron transport chain comprises an enzymatic series of electron donors and acceptors. Each electron donor passes electrons to a more electronegative acceptor, which in turn donates these electrons to another acceptor. This complex chemical reactions located in the inner mitochondrial membrane and is used to create a proton gradient across the membrane by pumping excess hydrogen ions into the mitochondria's "intermembrane space" [11]. In the electron transport chain, two proteins, NADH (nicotinamide adenine dinucleotide) [12] and FADH2 (flavin adenine dinucleotide) [13], are oxidized through a series of protein complexes, resulting in a release of protons. The

protons are then pumped into the intermembrane space using a portion of the energy released and create a proton gradient. Finally, these protons escape the intermembrane space through adenosine triphosphate (ATP) synthase [4], using the electric potential in conjunction with adenosine diphosphate (ADP) and inorganic phosphate. ATP is considered as cell's basic unit of energy. A change in the oxidation state of NADH and FADH2 is an indicator of a change in tissue bioenergetics [14]. Thus, we are interested in detecting these two proteins in the chain.

1.2.2 Oxidation in the Mitochondria

As explained earlier, the amount of oxygen present in and around the cell is one of the most important factors in regulating the mitochondrial production [15] and it has been shown that an irregularity in this amount of oxygen leads to cell death [16].

The excess or shortage of oxygen available to the cells is called oxidative stress, and shows a misbalance between the chemical compounds that the body produces and the body ability to consume it. These chemically reactive compounds contain oxygen and are called reactive oxygen species (ROS). ROS have important roles in cell signaling and homeostasis. An excessive amount of reactive oxygen species can result in the production of peroxides and free radicals, which may cause damage to all parts of a cell [17]. A variety of diseases can change the balance of oxygen flow into and around cells, and cause improper function of the mitochondria, and thus an increased rate of cell death, via apoptosis or necrosis [18]. Figure 1.3 shows the mitochondrial dysfunction, and cell death due to increasing oxidative stress [19].

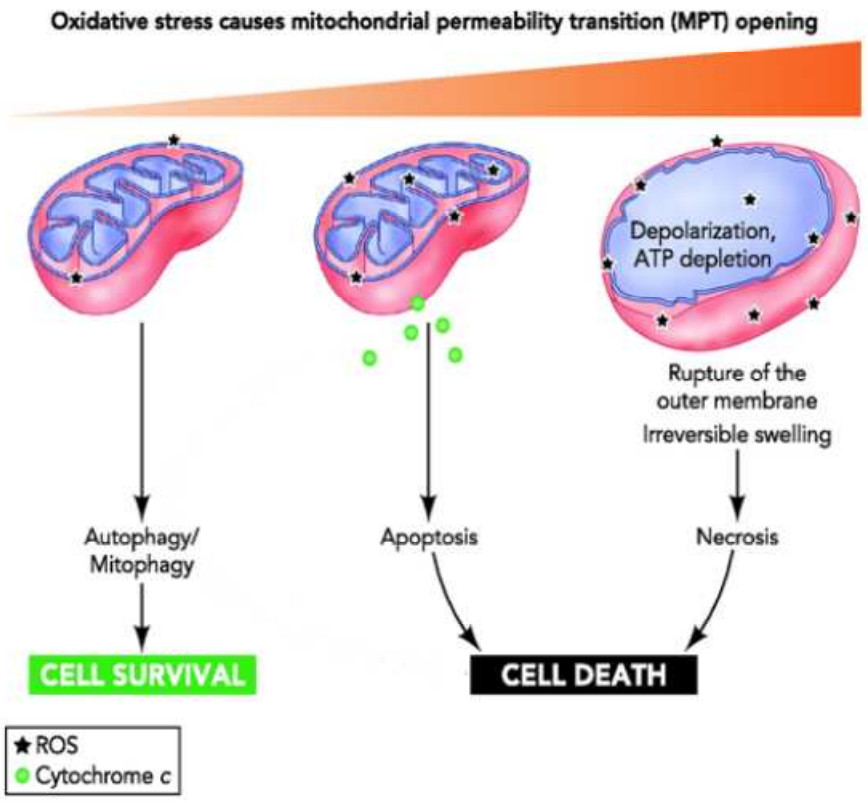

Figure 1.3: Impact of oxidative stress.

Mitochondrial dysfunction and cell death due to increasing oxidative stress [19].

In many cases the amount of oxygen available to a cell can accurately represent the health of the cell and be used as a tool for diagnosis. This is especially true in cases related to mitochondrial dysfunction or diseases related to oxidative stress, such as diabetes. In these cases, the oxidation state (redox state), of the tissue is a sensitive and reliable quantification for the cell behavior.

1.3 Fluorescence

1.3.1 Description of Fluorescence

Fluorescence is the emission of photons from a substance that has absorbed photons. In most cases the emitted light has a longer wavelength, and thus lower energy, than the absorbed photons [20].

Molecules are usually in the ground state. When the molecule is exposed to a source of energy such as a bright light source or high heat, it absorbs some of the energy and goes to an excited energy state. The amount of energy required to excite the molecule is large. Therefore, a light source is used for the excitation.

When the molecule at the excited energy state goes back to ground state, a small portion of the energy is lost to lattice vibrations prior to the release of extra energy. In the transition back to the ground state, there is a probability, termed the fluorescence quantum yield. Fluorescence quantum yield is defined as the ratio of the number of photons emitted to the number of photons absorbed. The maximum fluorescence quantum yield is 1.0 (100%), which means every photon absorbed is emitted. If the photon emission occurs, a photoelectric device can quantify the amount of releasing energy. This process can be seen in Figure 1.4 [21]. Jablonski diagram of fluorescence is another term used to show the aforementioned process.

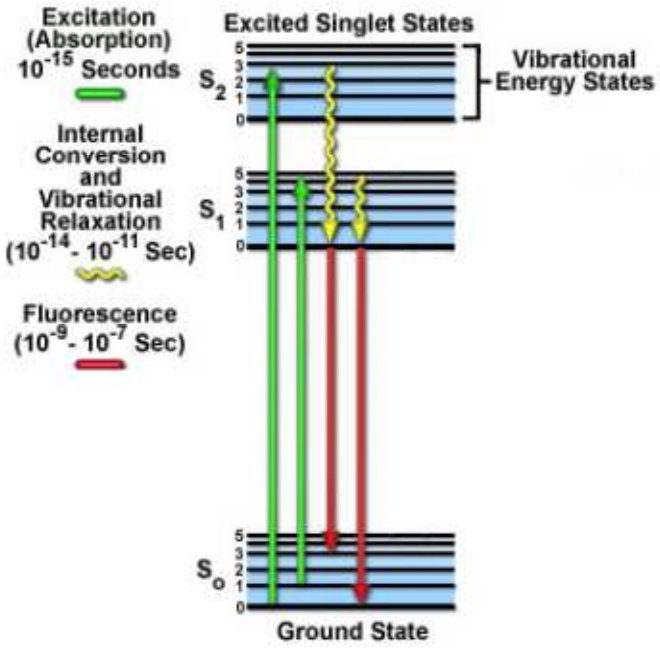

Figure 1.4: Jablonski diagram of fluorescence [21].

There is just a narrow range of light energies which can cause excitation corresponding to the allowed energy levels of the molecules, and especially intrinsic fluorophores. Based on the Planck relation, the energy of a photon is inversely proportional to its wavelength, or directly proportional to the frequency of the light. Thus, only a specific range of wavelengths can be used to excite a given molecule. The emitted fluorescence light also has a narrow range energy, so narrow wavelength and color equal to the energy released when the molecule transitions back to its ground state.

As explained earlier, some energy is lost between the time when the molecule leaves the excited state and returns to the ground state, which means excitation (absorption) and emission spectra must be different. This different shows a phenomenon known as the Stokes shift [22] and can be seen in Figure 1.5.

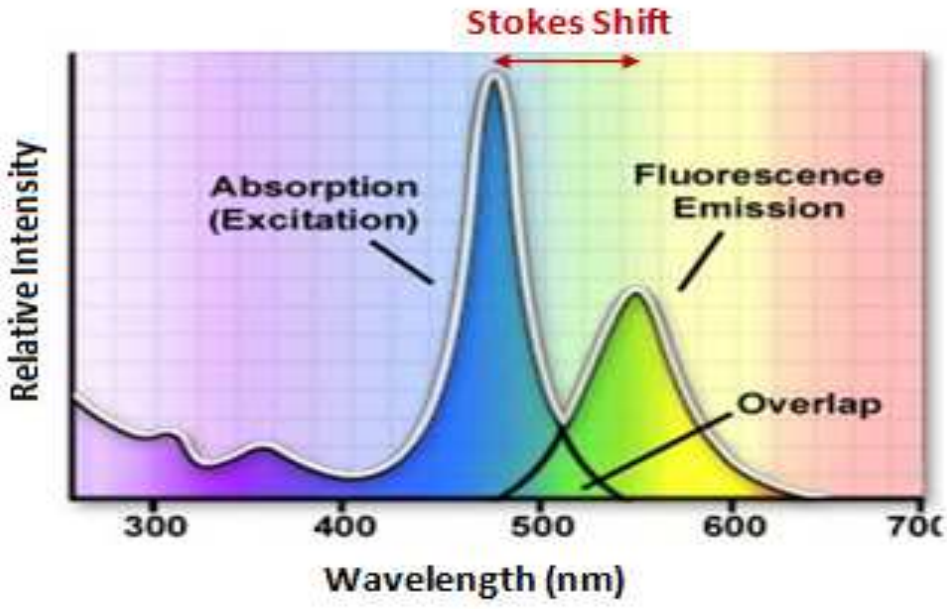

Figure 1.5: Stokes shift.

The difference between absorption and emission maxima is known as the Stokes shift [23].

This phenomenon can help us to separate the excitation and emission light by the use of optical filters or dichroic mirrors and only transmit the emission light to the detector of the devices which are able to measure the light.

1.3.2 Intrinsic Mitochondrial Fluorophores

Tryptophan, collagen, NADH, flavins, and porphyrins are some of intrinsic fluorophores in the tissue which can be considered as structural or physiological tissue parameters. NADH and FAD (one of the flavins) are the two proteins which we are interested in the most. They are autofluorescent coenzymes which are essential in the metabolic pathway of the mitochondria and help to determine the oxidation state of the

mitochondria [4]. The spectra of these two autofluorophores are shown in Figure 1.6 [24] [25] in some specific biochemical states [26]. NADH only fluoresces in its reduced form, whereas FAD only fluoresces in its oxidized form. Thus, the fluorescence signals from these fluorophores are used as indicators of tissue mitochondrial oxidation in injuries due to diseases. The ratio of these two fluorophores, called the mitochondrial redox ratio, is used as a marker of the oxidation state within the tissue [27]. Since, this ratio is independent of the number of mitochondria, thus, it is a better quantitative marker of tissue metabolism.

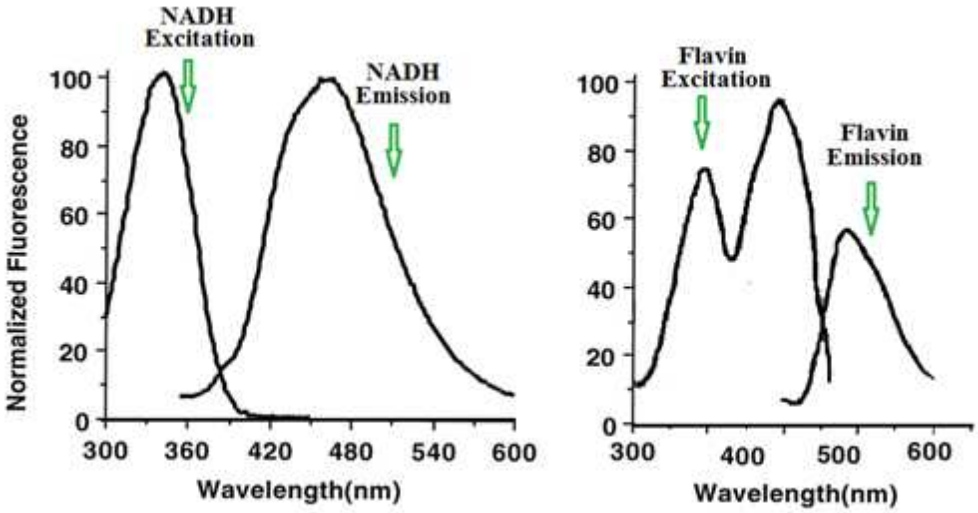

Figure 1.6: NADH and FAD fluorescence spectra.

Excitation and emission spectra of NADH (left) and FAD (right) .

In order to excite NADH and FAD, a white light such as mercury light is filtered at excitation wavelengths of these two coenzymes. The excitation spectrum of NADH has a peak value at 340 nm (ultraviolet region of the electromagnetic spectrum) and there is a

peak in the emission spectrum at 460 nm (blue in color). FAD has its excitation peak value at 448 nm (blue in color) and a peak value in the emission spectrum at 520 nm (green in color). As we can see, there is an overlap between NADH emission and FAD excitation which requires the two fluorophores be excited and detected sequentially.

As seen in Figure 1.6, the excitation spectra of the two fluorophores don't overlap each other, and the emission spectra don't overlap either. Hence, by detecting the fluorescence of each of these fluorophores, we can measure cellular metabolism of an organ.

Chapter 2

Cryoimaging-Macroscopy

2 Cryoimaging-Macroscopy

2.1 Introduction

The structure of organs and the redox ratio are both affected by disease progression. The changes in the mitochondrial redox state reflects physiological states that can be directly or indirectly related to structural changes. A high resolution 3D representation of the organ is essential to understand this relation [1]. In order to make a 3D representation, which gives enough information about the tissue, a high optical resolution imaging system (for microscopy purposes) with the capability of imaging all layers of the tissue is required. Cryoimaging is advantageous over the other methods because of the following reasons:

- It provides a strong fluorescence quantum yield of NADH and FAD as compared to room-temperature imaging techniques. The stronger signal, the higher signal to noise ratio and the more accurate measurement.
- It demonstrates 3D spatial distribution of NADH and FAD fluorescence intensities in tissue.
- It provides the snapshot of metabolism at the freezing time.

In the following chapter the cryoimager of Biophotonics Lab at University of Wisconsin-Milwaukee is described in macroscopy setup for tissue redox calculations (version 1) and in the next chapter, the microscopy setup, which I added to the system, (version 2) for high resolution 3D tissue structure presentation will be explained in detail.

2.2 Cryoimager

The cryoimager is an automated image acquisition and analysis system consisting of software and hardware designed to acquire fluorescence images of tissue sections [28] [29]. This device uses the autofluorescence of the previously mentioned NADH and FAD co-enzymes within the mitochondria to determine the cellular redox state. By measuring the fluorescence intensities of a reduced protein, NADH, and an oxidized protein, FAD, one can obtain an effective measure of the oxidation state of the mitochondria.

We use this device to monitor the autofluorescence of the NADH and FAD co-enzymes within the mitochondria to determine the cellular redox state. By measuring the fluorescence intensities of a reduced protein, NADH, and an oxidized protein, FAD, one can obtain an effective measure of the oxidation state of the mitochondria.

The cryoimager has a motor-driven microtome, which sequentially sections frozen tissue. The thickness of sections which defines the resolution in z direction is adjustable. This resolution can be as small as 5 μm. A broadband light from a mercury arc lamp is filtered by a filterwheel with up to five distinct fluorophores filters. The filtered light is then reflected and exposed to the surface of the tissue block. After each slice, a CCD camera records a fluorescence image of the tissue block after the emitted backlight passes through another filterwheel and an optical lens. Later the stacks of images will be analyzed to determine the fluorophore distribution. The microtome of the cryoimager is housed in a freezer unit with a temperature around -25°C during sample slicing and image acquisition.

2.2.1 Hardware Components

The cryoimager consists of some main components like a freezer, blade (including all mechanical devices participating in slicing process), mercury arc lamp, cold mirror and reflecting mirror, excitation and emission filterwheels, lenses, and camera.

Except the freezer and the blade (which is located inside the freezer) all other mentioned components are parts of two main light paths, namely the excitation light path and emission light path, which will be explained in the following sections.

2.2.1.1 Microtome Blade

The cryoimager contains a blade which is driven by an AC motor (Blador, 1/3 HP AC motor VL 3501). The blade and the motor are housed in the cryoimager freezer container. The movement of the blade is controlled through an implemented software with the help of two sensors located on top of the blade holder. Figure 2.1 shows the blade and the two sensors.

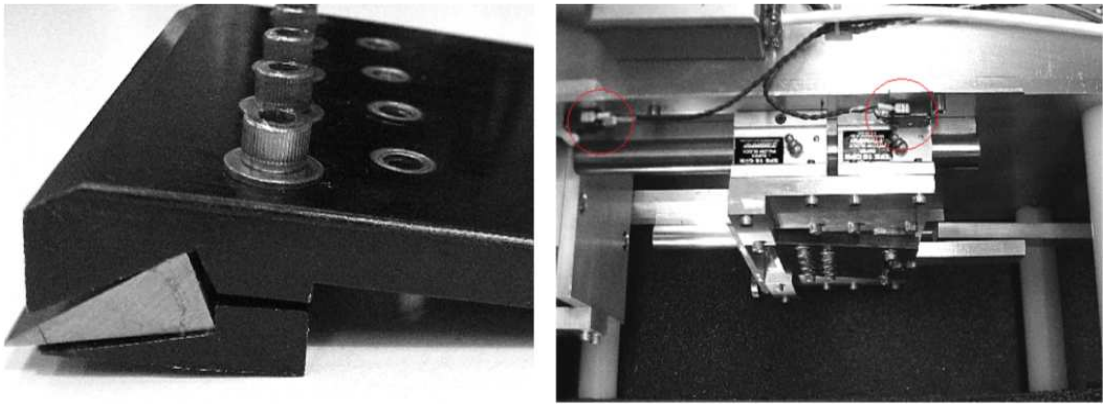

Figure 2.1: Microtome blade.

left) Blade and blade mount. Right) Blade mount and sensors in the freezer.

2.2.1.2 Ultra-Low Freezer

The cryoimager includes an ultralow freezer, in which the inside temperature is controlled by an interchangeable temperature sensor. The temperature goes down to -25°C while slicing and imaging.

2.2.1.3 Filterwheels

Two optical filterwheels (named excitation and emission filterwheels) rotate simultaneously to provide required excitation/emission wavelengths for fluorescence imaging. The excitation filterwheel is located after the excitation light source and the emission filterwheel is located after the sample. Both filterwheels are controlled by stepper motors and their drivers through the implemented software.

2.2.1.4 Camera

We usually use the two following cameras:

- Exi Aqua (QImaging EXi Aqua, Canada): This is a color CCD Camera with low dark current and high quantum efficiency. The pixel size is 6.45um*6.45um and the CCD size is 1392*1040 pixels [30].
- Rolera (QImaging, EM-C2 Rolera, Canada): This is a monochrome camera, which features lower noise and more sensitivity in terms of signal detection. The pixel size is 8um*8um and the CCD size is 1004 * 1002 pixels [31].

The Aqua camera has a smaller CCD pixel which helps imaging in higher resolution, while the Rolera camera has a higher signal to noise ratio and works better in dark environments.

2.2.1.5 Lamp

The lamp used in cryoimager is a 200 Watt mercury-arc lamp (Number 6283NS, Newport Instrument, CT, US).

This type of lamp has a broadband, intense white light, which is able to excite multiple fluorophores. The spectrum of the lamp is shown in Figure 2.2. As seen this type of lamp has two intense spectral peaks at 365 nm and 436 nm, which correspond to the excitation peaks of NADH and FAD respectively.

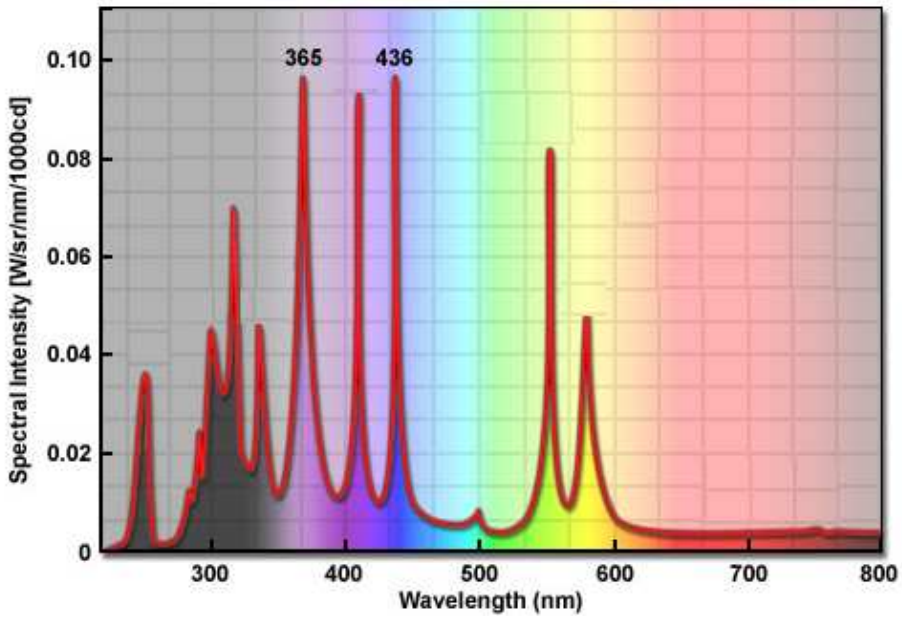

Figure 2.2: Spectral intensity of mercury-arc lamp.

2.2.2 Light Paths

2.2.2.1 Excitation Path

The broadband, intense white light, generated from the mercury-arc lamp is considered as excitation light. This light is coupled into a condenser, which homogenizes the light. The light is then incident on a cold mirror. The cold mirror eliminates the infrared portion of light.

The homogeneous light then passes through a filterwheel called the excitation filterwheel. The filterwheel contains a set of optical band-pass filters to filter the light at the proper wavelengths of fluorophore excitation.

The filters used in our research attenuate the light by approximately five orders of magnitude out of the nominal bandwidth. The excitation band-pass filter used for NADH is 350 nm with an 80 nm bandwidth, (UV Pass Blacklite, HD Dichroic, Los Angeles, CA) and for FAD is 437 nm with a 20 nm bandwidth, (440QV21, Omega Optical, Brattleboro, VT).

The narrow-range excitation light at the desired wavelengths is then reflected by a mirror, and finally illuminates the tissue surface inside the freezer unit. Figure 2.3 shows the excitation path of the cryoimager.

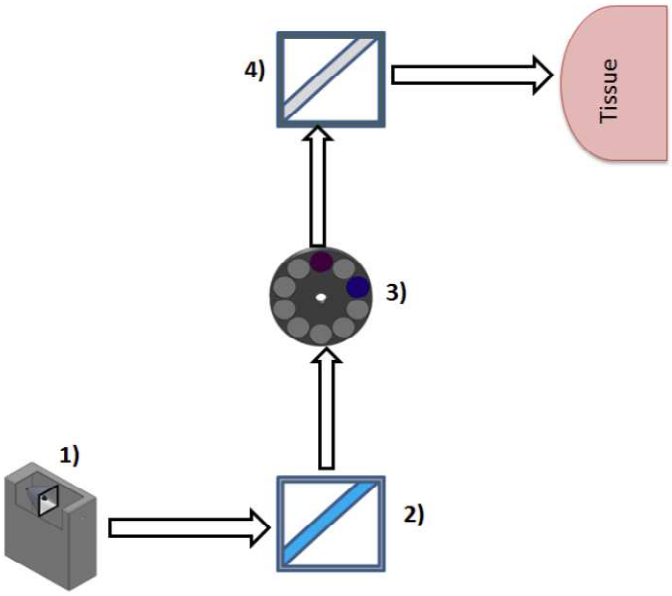

Figure 2.3: Cryoimager excitation path schematic.

1) Mercury-arc lamp. 2) Cold mirror. 3) Filterwheel. 4) Reflecting Mirror.

2.2.2.2 Detection Path

After light is exposed on the tissue surface, the autofluorophores FAD and NADH emit fluorescence light. This light passes through another filterwheel and a lens. The order and the types of the filterwheel and the lens vary due to the desired magnification and resolution of the final images. Finally, a CCD camera records a fluorescence image of the tissue block to be later analyzed for fluorophore distribution.

We used to use a certain lens and filterwheel setup in the detection path namely the macroscopy. I implemented and added a new setup for microscopy purposes to the cryoimager. Both setups are described in further detail below.

2.2.2.3 Cryoimaging-Macroscopy Setup

In this setup, the light emitted from the tissue sample passes through a fixed large filterwheel containing filters with 2 inch diameter, then a lens, and finally the camera. The lens used in this setup is a Canon standard lens (EF 28-135 mm, f/3.5-5.6 IS) with low distortion and a large aperture. The large aperture of the lens and the large filters collect more light (than if a small aperture and filters were used) from the sample and compensate for light dispersion and dissipation at this setup.

The filter used for NADH is 460 nm (50 nm bandwidth, D460/50M, Chroma, Bellows Falls, VT) and for FAD is 537 nm (50 nm bandwidth, QMAX EM 510-560, Omega Optical, Brattleboro, VT). We use this setup to image samples in cryo-macroscopy and usually in one field of view. Figure 2.4 shows this emission light path setup, used mostly in cryo-macroscopy.

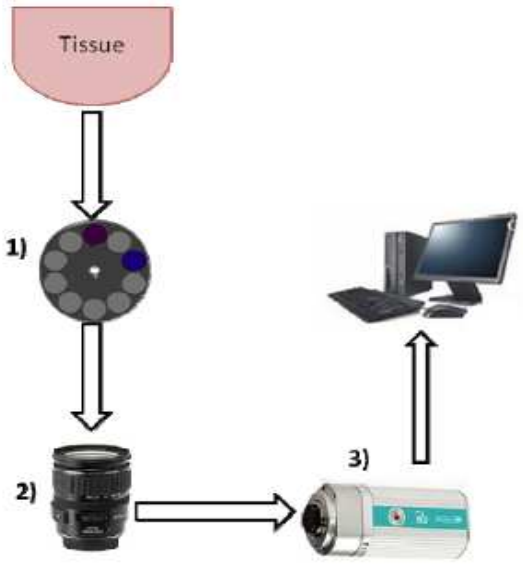

Figure 2.4: Cryoimager detection path schematic, macroscopy setup.

1) Emission bigger size filterwheel. 2) Canon lens. 3) Aqua Exi camera.

2.2.2.4 New Cryoimaging-Microscopy Setup

In this setup, the emitted light from the tissue sample first passes through a zoom lens, then a small filterwheel, containing filters with 1 inch diameter, and finally the camera. The lens is an Optem Zoom lens system (125C 12.5:1 Micro-Inspection, Qioptiq) and the filter used for NADH is 445 nm (90 nm bandwidth, HQ 445/90M, Chroma, Bellows Falls, VT) and for FAD is 520 nm (35 nm bandwidth, FF01-520/35-25, Semrock, Rochester, NY). This zoom lens has a large focal length with a slim body in respect to the Canon lens. Therefore, a small filterwheel is used in between the camera and the lens. Placing the filterwheel in between the lens and the camera gives us the freedom to move the lens closer to the sample, and collect more light before it dissipates from travelling in the air. We use this setup for microscopy imaging (high resolution imaging), where we need more details of the tissue samples. Figure 2.5 shows this emission light path setup, used in cryo-microscopy. Implementing this setup required some modifications in different parts of the cryoimager, which will be explained in next chapter.

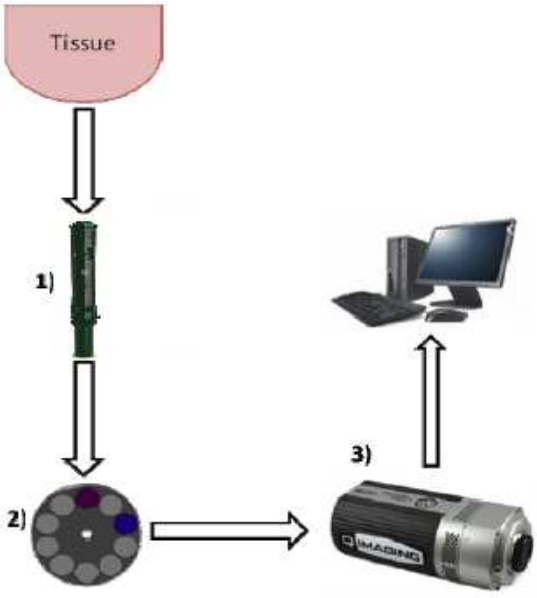

Figure 2.5: Cryoimager detection path schematic, microscopy setup.

1) Optem zoom lens. 2) Emission small filterwheel 3) Rolera EM-C2 camera.

2.2.2.5 Entire System

Figure 2.6 shows the schematic and the physical implementation of the cryoimager with the two different detection paths. In summary, the light path begins with the mercury-arc lamp, and then passes through a coupled cold mirror. The light then passes through the excitation filterwheel, where the desired wavelengths of light are selected. This light is then reflected to the tissue via a reflecting mirror. The emitted fluorescent light from the tissue then passes through the emission filterwheel and lens, and will be finally captured by the camera.

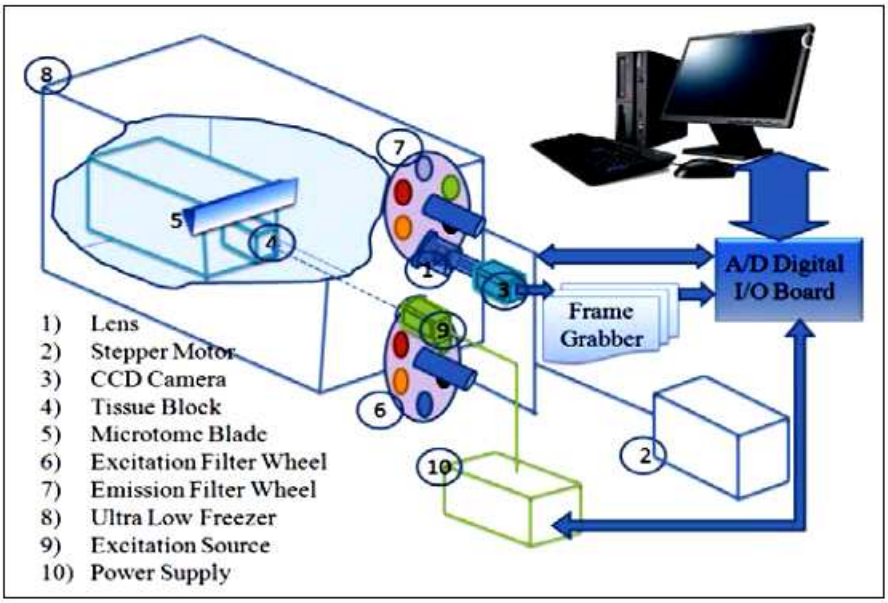

Figure 2.6: Cryoimager schematic.

2.2.3 Software

To control the slicing and image acquisition process, a software is implemented in LabVIEW. The software is also responsible for controlling different settings, such as adjusting the camera settings (gain and exposure), setting up the file format and location, adding filters to the experimental setup and rotating the filterwheels, positioning the sample (moving the sample block surface to the location where the blade is able to cut at the desired thickness), setting the slices thickness, and controlling the automated image acquisition. As soon as the aforementioned parameters are set, the slicing and imaging process can be started. Figure 2.7 shows the slicing and imaging sequence of the cryo-macroscopy.

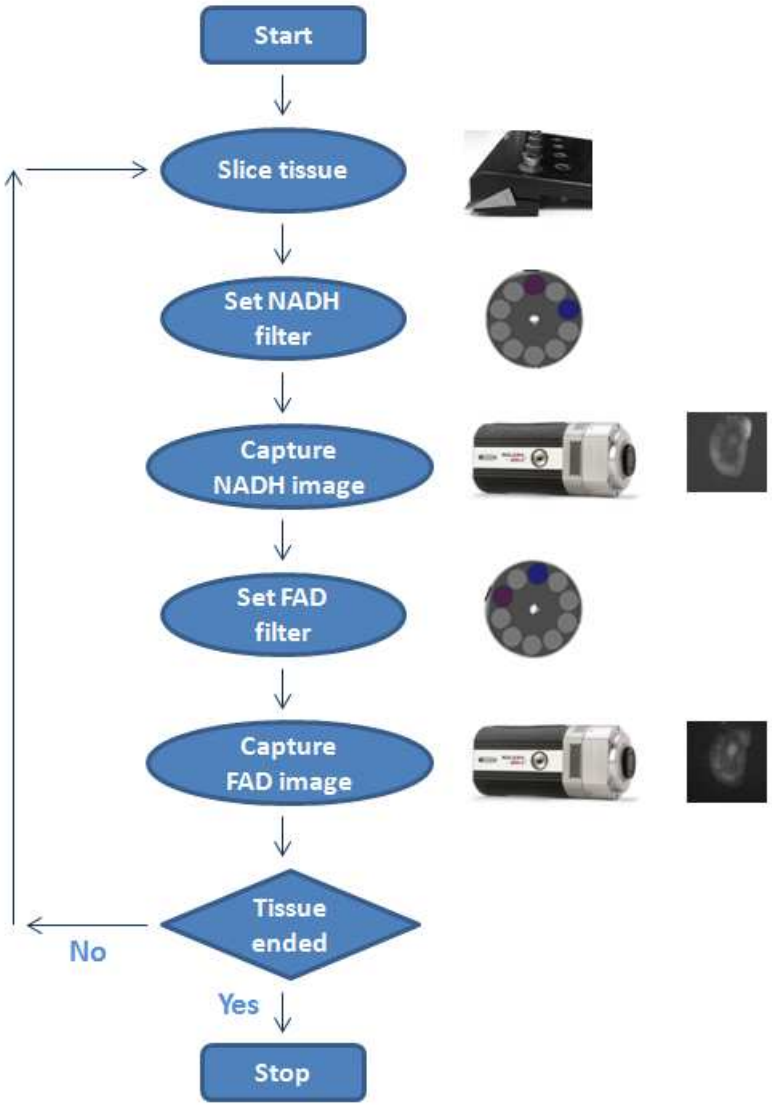

Figure 2.7: Cryoimager slicing and imaging sequence.

2.2.4 Sample Preparation

Before a sample is ready for cryoimaging, there are several steps that must be taken. These include tissue preparation, sample freezing, mounting medium preparation, and sample embedding.

After the desired tissue or organ sample (controlled, diseased or special tagged) is harvested, in order to preserve tissues metabolic state, the sample should be frozen. We immerse the sample in chilled isopentane (2-methyl butane, -80°C) for 1-2 minutes for primary freezing and then place it in liquid Nitrogen (LN2). This method prevents the sample from cracking due to sudden temperature changes. Frozen tissues can be stored in a LN2 Dewar or an ultralow freezer (-80°C) to be imaged later. The sample will be embedded in a black mounting medium, which is fluorescent free at the excitation wavelengths of interest. Polyvinyl alcohol, distilled water and carbon black powder or India ink are used to make a reliable fluorescent-free mounting medium. The frozen sample is placed on a bed of frozen black mounting medium on top of a metal plate, and then covered with more black mounting medium. The whole sample block will be allowed to rest in the ultralow freezer for a day before imaging. Finally, the metal plate will be mounted on the sample carriage in the cryoimager, ready to be sliced and imaged. Figure 2.8 shows a kidney during mounting.

Figure 2.8: Sample embedding.

Left) Sample on the mounting medium. Right) Sample block ready for cryoimaging.

2.2.5 Image Processing

MATLAB and ImageJ are the two main software platforms used for image processing and 3D rendering, respectively (although, both platforms have the capability to perform the two mentioned applications). LabVIEW is also used to stitch the images taken in microscopy. In the following sections, first the pre-processing steps including image calibration will be explained. Then the stitching algorithm implemented in LabVIEW to construct cryo-microscopy images is discussed, and finally the post-processing and different presentations of data are illustrated.

2.2.5.1 Pre-processing

Before processing we should make sure to remove any undesired images from the stack of images. These images, for instance, could be the ones in which the black mounting medium after being sliced is folded and stuck to the tissue surface, affecting the next image. This problem, as illustrated in Figure 2.9, occurs frequently when we take very thin slices of the tissue sample (around 10 to 15 um).

Sometimes we also need to compensate for the sudden increase or decrease in light intensity in the middle of an experiment, as shown in Figure 2.10 . This can be caused by the user in an attempt to prevent saturation or improve the contrast of the image.

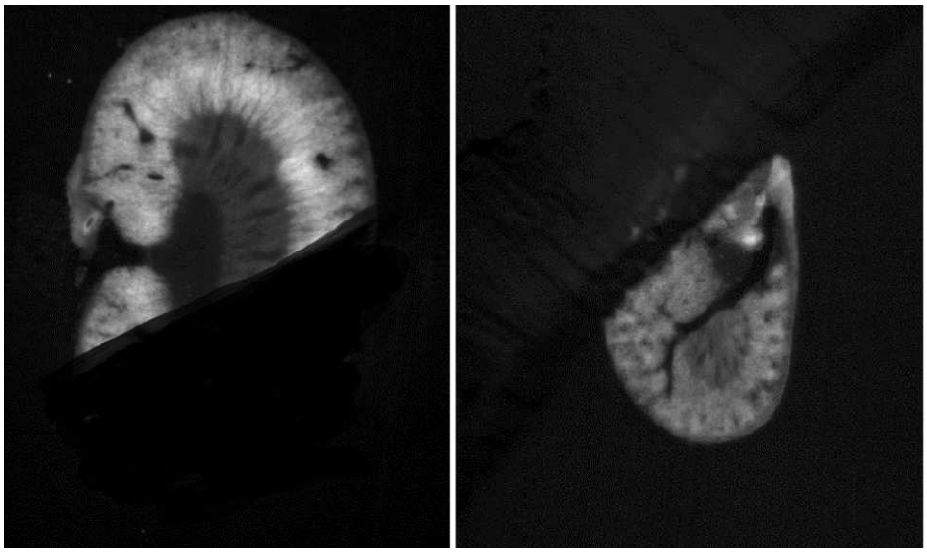

Figure 2.9: Undesired sample slices.

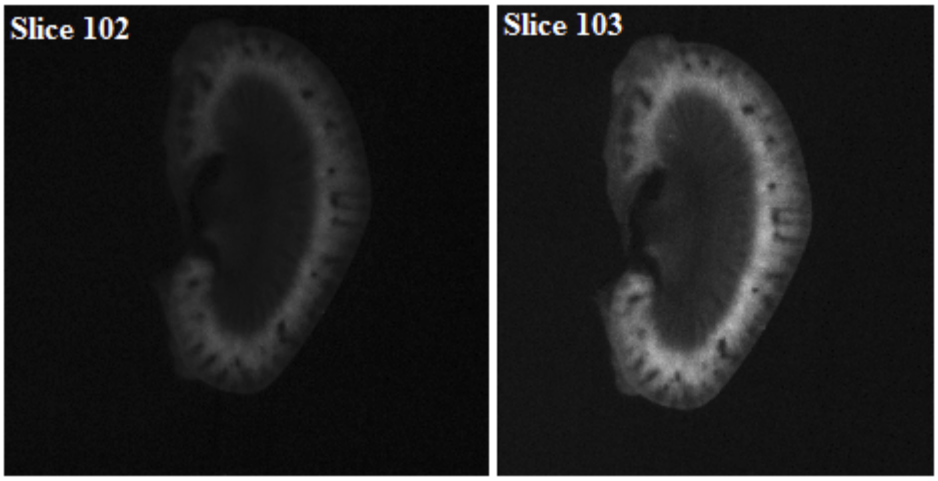

Figure 2.10: Intensity change in two consecutive NADH images.

2.2.5.2 Imaging Calibration

Calibration is an important part of imaging. For each experiment, we acquire several calibration images to compensate for day-to-day variations of light intensity and non-uniformity of the illumination pattern. Figure 2.11 shows a set of calibration images

taken at the beginning of each experiment and before slicing the tissue. Figure 2.11 (1) shows image of a grid. This image is used to determine the magnification of the images and to set the focus of the lens. The dimension of each small square in the sample grid paper is 1 mm and the real magnification can be easily defined by the size of the camera CCD. Figure 2.11 (2) is a sample dark current image. This image is used for background subtraction. Figure 2.11 (3 and 4) show the flat-field images in NADH and FAD channels respectively. The flat-field image is captured from a uniformly fluorescent and flat object. It accounts for day-to-day light intensity variations as well as possible non-uniform distribution of light on the sample. All the images in each channel were then normalized by dividing each image to the flat-field image captured in the same channel.

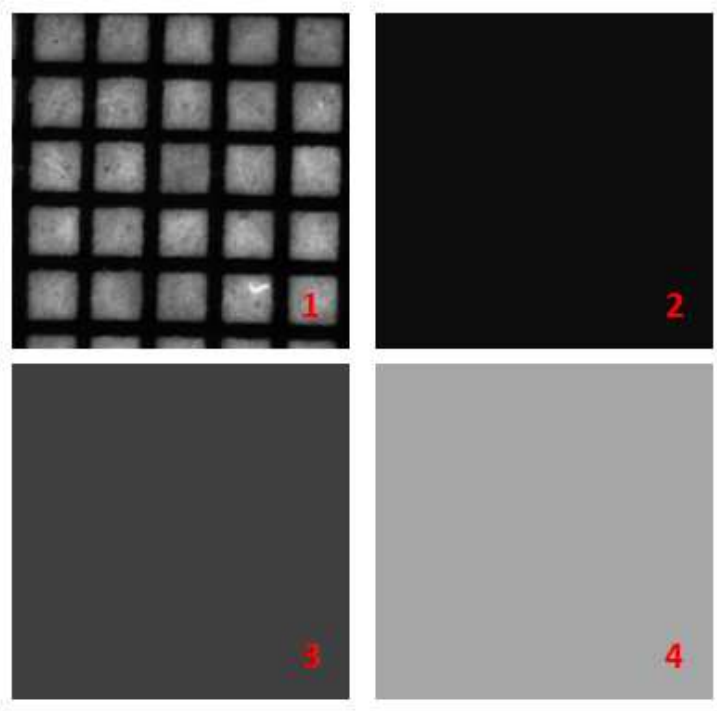

Figure 2.11: Calibration Images.

1) Grid image 2) Dark current image 3) NADH channel flat field image 4) FAD channel flat field image.

2.2.5.3 Post-processing

2.2.5.3.1 Redox calculation in MATLAB

After pre-processing, FAD and NADH images of the samples (taken in either macroscopy or microscopy) are loaded into MATLAB, and background correction and exposure compensation are performed.

NADH fluorescence images are then divided by the corresponding FAD images, voxel by voxel, to calculate the NADH redox ratio for each slice of the tissue sample, and the redox stack is constructed. The final results can then be presented in one of the following methods, depending on the organ and desired part of the tissue.

One Slice Representation

In this method, one representative slice from the whole sample is chosen to display the results. Figure 2.12 shows NADH, FAD, and NADH redox images from one slice of a control mouse kidney, which shows one cross-section of the tissue. This method is used when emphasizing a specific part of the tissue which is of most interest.

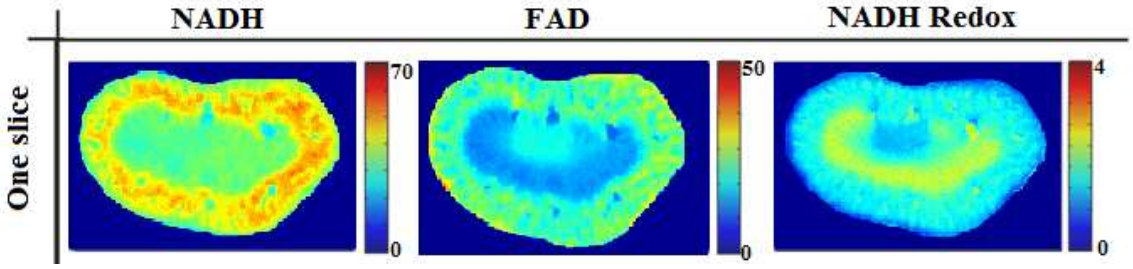

Figure 2.12: One slice method data representation.

NADH, FAD, and NADH redox images of a control mouse kidney.

Whole Volume Representation

In this method, we form a composite image using all slices in NADH, FAD, and NADH redox. These 3-D composite images are used for representation and comparison of the data and calculation of the histograms. Figure 2.13 shows the rendered NADH and FAD images and the redox volume calculations of a control mouse kidney.

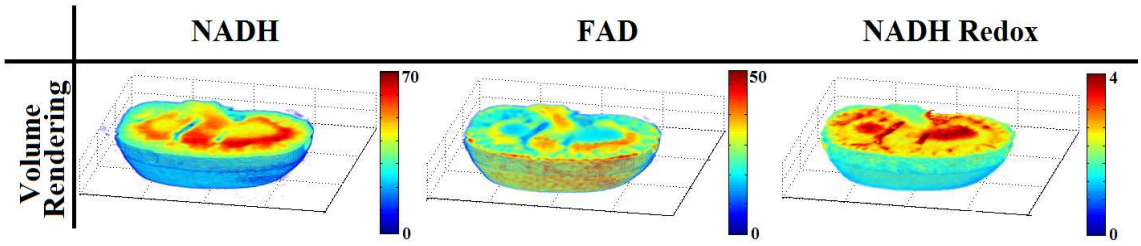

Figure 2.13: Whole volume method data representation.

NADH, FAD, and NADH redox images of a control mouse kidney.

Maximum Projection Representation

In this method, the maximum intensities along the z-axis of the composite images 3D volume in NADH, FAD, and redox ratio) are calculated and used for representation and comparison of the data. Figure 2.14 shows the maximum projection of NADH, FAD, and NADH redox in a control mouse kidney.

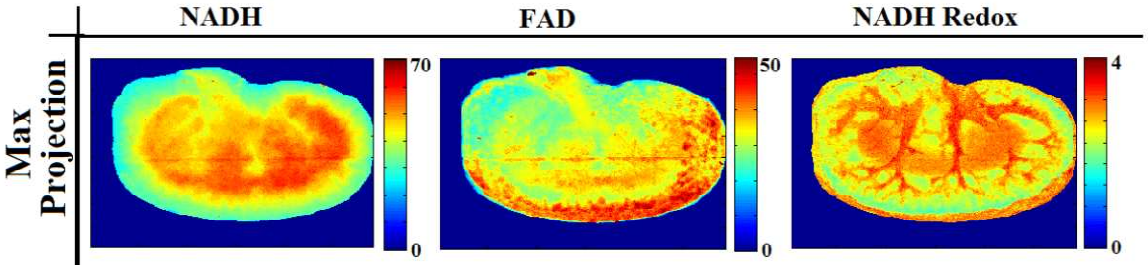

Figure 2.14: Maximum projection method data representation.

NADH, FAD, and NADH redox images of a control mouse kidney.

2.2.5.3.2 3D visualization in ImageJ

The 3D viewer plug-in of ImageJ is used to present the structure of the tissues. This plug-in allows us to display stacks of images as volume renderings or surface plots, and enables us to perform volume editing. Figure 2.15 shows an example of a 3D rendering with this software.

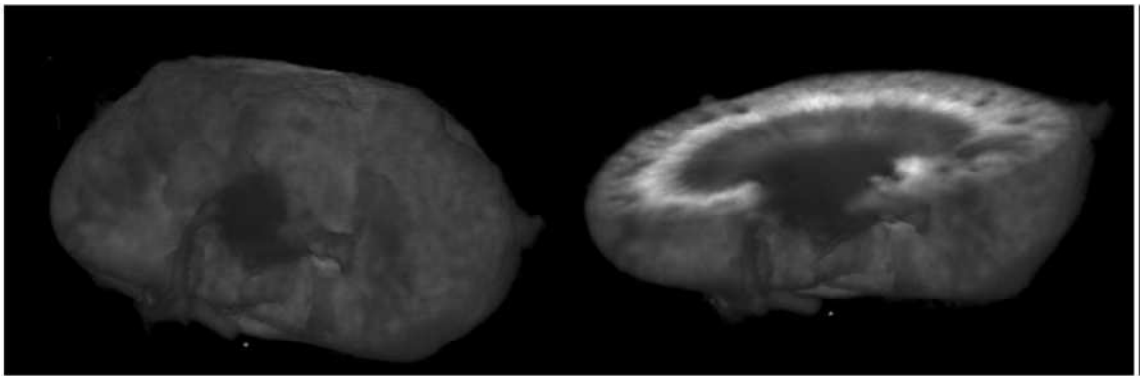

Figure 2.15: 3D rendering of a control mouse kidney sample reconstructed in ImageJ.

Whole and half kidney.

Chapter 3

Design and Implementation of

Cryoimaging-Microscopy

3 Design and Implementation of Cryoimaging-Microscopy

3.1 Introduction

As explained earlier, one of the main goals of this research is to represent the small structures of the tissue samples in 3D, look at the changes in the structure due to the diseases, and compare the results with the redox ratio. Cryo-microscopy seems to be the best approach to this goal. But at the same time microscopy has led to some limitations and challenges in imaging, and we needed to modify our cryoimager for microscopy. These limitations and challenges are summarized into three categories and are explained in the following subsections.

3.2 Microscopy Imaging Challenges

3.2.1 Resolution

Due to some optical system limitations (specifically lack of resolution), magnifying an image for microscopy does not always show the details we are looking for. The resolution of an image is the detail an image holds. Higher resolution means more image detail. Resolution is defined in number of line pairs per millimeter (LP/mm). Each pair consists of a black line and a white line. In other words each LP/mm is equal to 2 lines per millimeter. Higher LP/mm means higher image resolution [32] [33].

For high-resolution imaging we need an optical system with high optical resolution. Optical resolution is the ability of an imaging system to resolve detail in the object that is being imaged. Imaging systems may have different individual components like filters, lens mechanism, and recording and monitoring devices. Each of these components, plus the environment in which the imaging is done, contributes to the final optical resolution of the system [34]. In this research, we particularly focus on the lens.

To transition from cryo-macroscopy to cryo-microscopy, we have to use a special lens to be able to magnify the sample while having high optical resolution.

There are two main parameters that should be taken into consideration for choosing a lens with desired resolution.

- Numerical aperture.
- Working distance.

The light-gathering ability of a lens is expressed in terms of the numerical aperture, which is a measure of the number of highly diffracted image forming light rays captured by the lens. Higher values of numerical aperture allow increasingly oblique rays to enter the lens, producing a more highly resolved image [35].

Working distance, the distance from the sample to the camera CCD surface, will be explained in further detail as a part of the cryo-microscopy implementation.

As mentioned earlier, we used an Optem Zoom lens system (125C 12.5:1 Micro-Inspection, Qioptiq). This lens is capable of magnifying the image up to 6.5X without any auxiliary lens. With an auxiliary lens of 2X, it can magnify up to 13.0X without changing the main tube of the lens [36]. The lens is shown in Figure 3.1.

Figure 3.1: Optem zoom lens.

This lens is used for cryo-microscopy.

The resolution, numerical aperture, and working distance of the Optem lens at different magnifications, without and with 2X auxiliary lens, are shown in Table 3-1 and Table 3-2.

1X main tube with no auxiliary lens	**Low magnification**	**High magnification**
Magnification Range	0.52X	6.5X
Resolution	58 LP/mm	300 LP/mm
Numerical Aperture	0.019	0.10
Working Distance	89 mm	

Table 3-1: Optem zoom lens specifications with no auxiliary lens.

1X main tube with 2X auxiliary lens	Low magnification	High magnification
Magnification Range	1X	13X
Resolution	114 LP/mm	594 LP/mm
Numerical Aperture	0.038	0.20
Working Distance	32 mm	

Table 3-2: Optem zoom lens specifications with 2X auxiliary lens.

3.2.2 Chromatic Aberration

As explained in Chapter One, we usually analyze the concentration and distribution of the two coenzymes FAD and NADH in the tissue samples. To do this, we image in two channels of the cryoimager by using appropriate filters for FAD and NADH excitation and emission wavelengths.

Before starting the imaging and while performing the pre-imaging setup, we adjust the lens to focus on one channel. If we change the channel to the other without refocusing, we see the new images become blurry. This is the result of an optical phenomenon called aberration. Figure 3.2 shows aberration in the images taken by the cryoimager with the Canon lens and in cryo-macroscopy configuration. At the picture we see a slice of control mouse kidney sample with FAD channel in focus. Because of the

aberration the NADH channel is out of focus. The number of girds in the grid image of Figure 3.2 shows the images are taken in macroscopy.

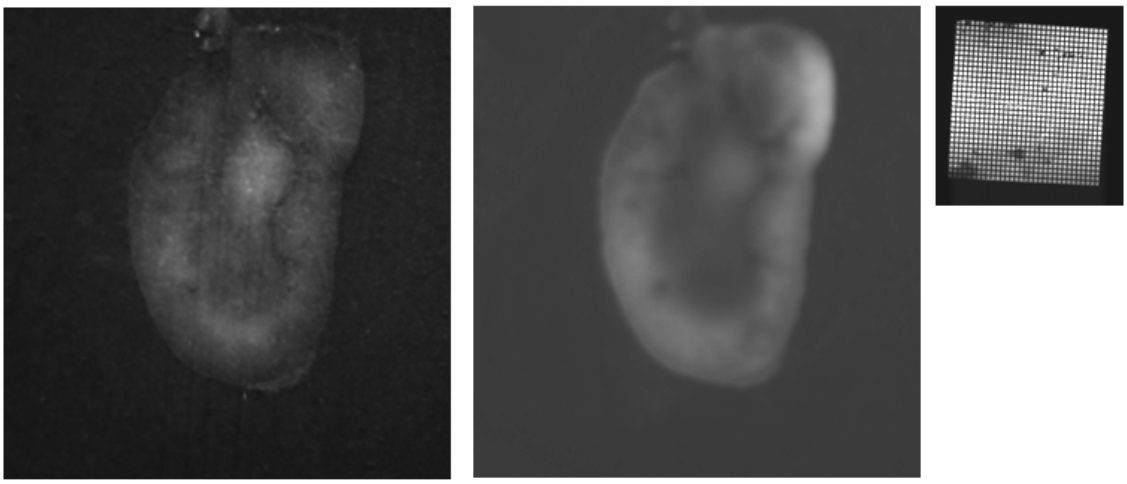

Figure 3.2: Chromatic aberration in Canon lens, rat kidney sample.

Left) FAD channel. Right) NADH channel. While the FAD channel is in focus, the NADH channel is out of focus.

It is clear that blurry images suppress detailed information about the distribution of NADH and FAD and therefore the redox ratio. So, the goal is to cancel the effect of the aberration on the captured images to preserve the information within the images which helps us to quantify redox ratio and represent tissue structures.

Aberration is due to flaws in optical elements, and it results in blurring and distortion in the image taken.

In an imaging system, aberration occurs when visible light from one point of an object does not converge into a single point after passing through the system [37, 38].

Aberrations are divided into two classes:

- Monochromatic aberration
- Chromatic aberration

3.2.2.1 Monochromatic Aberration

The geometry and the nature of a lens, including spherical, coma and curvature is the cause of this type of aberration. It occurs when light is either reflected or refracted and all beams of light do not converge to the focal point of the lens. It appears even when monochromatic light (visible light with a narrow band wavelength) passes through the lens [39].

3.2.2.2 Chromatic Aberration (Achromatism)

Chromatic aberration occurs when a lens is not able to focus all colors (wavelengths) of the light to the same convergence point because it has different refractive indices for different wavelengths of light. In a lens, higher wavelengths have a lower refractive index [39]. With chromatic aberration, images are distorted and are blurry.

There are two types of chromatic aberration:

- Axial (longitudinal)
- Transverse (lateral)

3.2.2.2.1 Axial (longitudinal)

Axial chromatic aberration occurs when different wavelengths of light focus at different distances from the lens on the optical axis. This type of aberration is also called focal shift.

3.2.2.2.2 Transverse aberration (lateral)

Transverse chromatic aberration occurs when different wavelengths of light focus at different positions in the focal plane of the lens.

To reduce the chromatic aberration, lens manufacturers usually use the following techniques:

- The focal length of the lens is increased to the maximum possible length.
- An achromatic lens, or achromat, is used to reduce the chromatic aberration. In these lenses materials with differing dispersions are used to make a compound achromatic lens.
- Combining more than two lenses of different composition can increase the degree of correction further. This technique is used in an apochromatic lens, or apochromat.
- Costly fluorite glasses with very small tolerances are used to make superachromat lenses. In this lens four separate wavelengths can be brought to focus in the same plane.

Figure 3.3 visualizes the two different chromatic aberrations versus an ideal lens which is considered to be aberration free [40].

Figure 3.4 shows the focus error (focal shift) of different types of lenses versus different wavelengths [41].

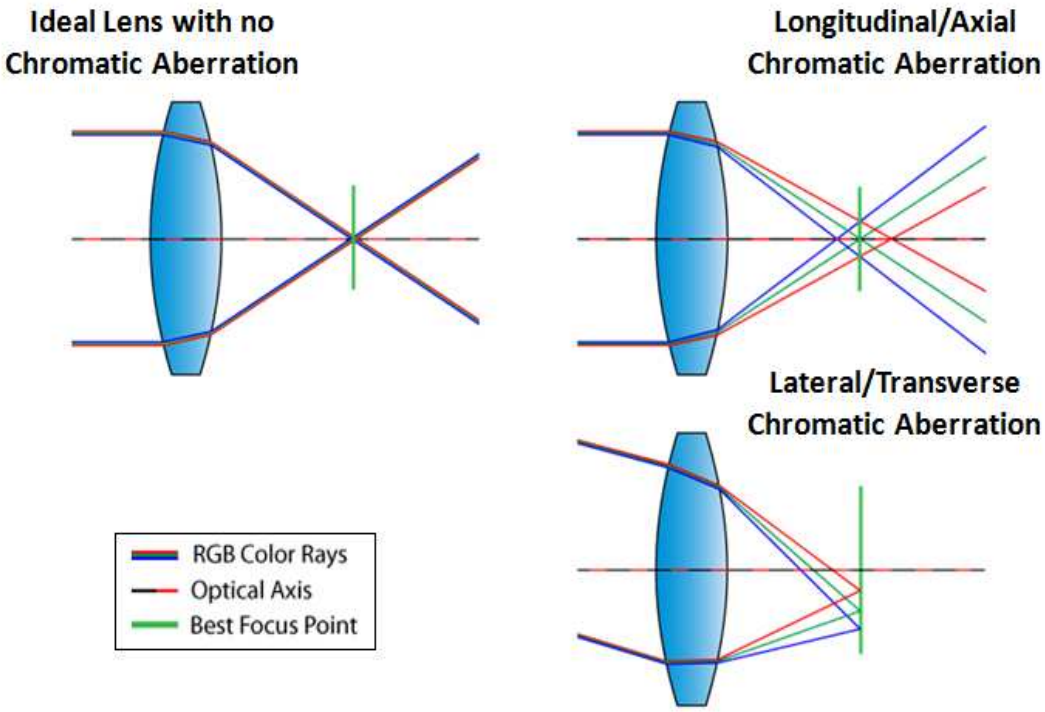

Figure 3.3: Axial and transverse chromatic aberration versus an aberration free lens [40].

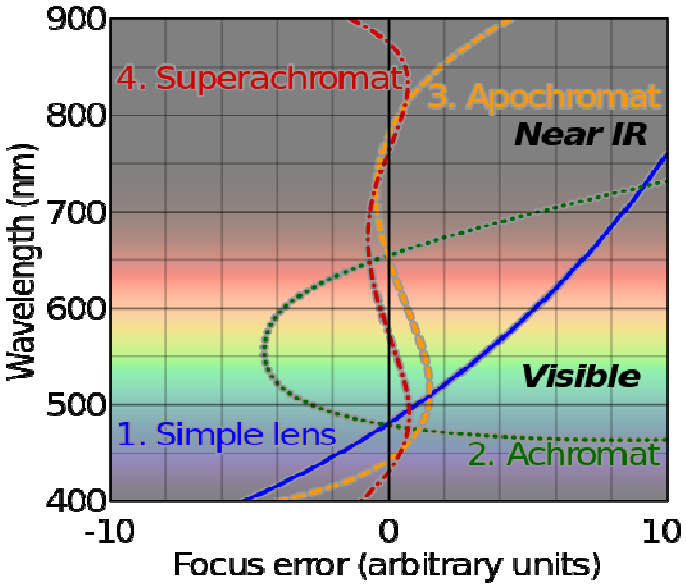

Figure 3.4: Chromatic correction of visible and near infrared wavelengths [41].

1) Simple, 2) Achromatic doublet, 3) Apochromatic, and 4) Superachromat.

Although lens manufacturers apply these techniques to reduce chromatic aberrations, chromatic aberration is still an issue on most prime and zoom lenses, and affects many images especially at higher resolution imaging. In Section 3.3.2 the method I have used to eliminate chromatic aberration is explained.

3.2.3 Field Of View

The area that is visible to an optical instrument is called the field of view (FOV). By increasing the magnification, the field of view decreases and vice versa. In other words, in order to be able to see the tissue structure, we have to increase the magnification, which results in a smaller field of view. As a result, imaging the whole tissue samples in high resolution in just one field of view may not be possible, and only a small part of a large sample would be captured like the one shown in Figure 3.5 [42]. Since we are interested in imaging the whole tissue sample, regardless of size, a raster scanning mechanism is implemented which will be explained in subsection 3.3.3.

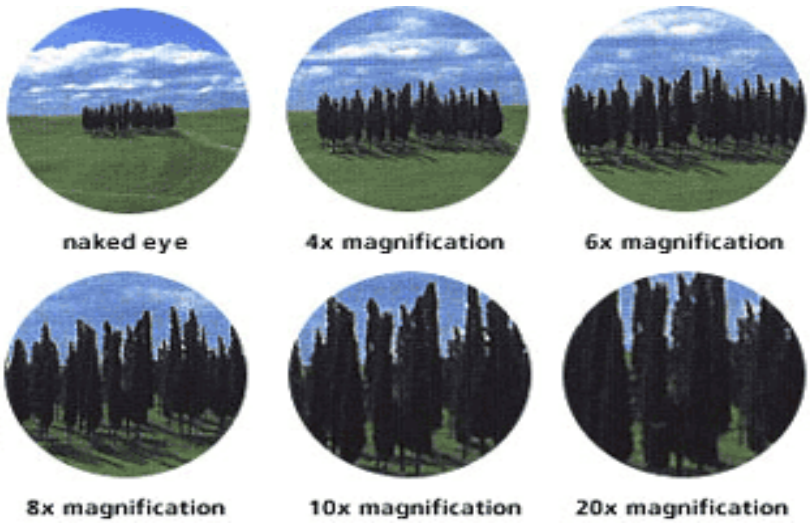

Figure 3.5: Scenery at different magnifications [42].

3.3 Implementation of Cryo-Microscopy

In the previous section, the challenges in cryo-microscopy were explained. In this section the solutions and the implementations done to overcome the challenges are explained. Based on the main requirement of cryo-microscopy, which is recording images in high magnification, the importance of an aberration-free lens mechanism with a long working distance is apparent. We searched the market for a lens with the aforementioned properties, and the best choice applicable to our cryoimager was Optem zoom lens. Some detailed information about this lens was already given. In the following section, more information about other properties of this lens will be given in the following section.

3.3.1 Long Working Distance Lens

By increasing the magnification, the working distance of any lens decreases, which means the lens should be closer to the sample being imaged. Since there was a long distance between the location of the sample in the freezer and the location of the camera and lens, we had to decrease this physical distance and bring the sample into the lens' working distance for cryo-microscopy. By some modifications in the cryoimager setup, we could decrease the distance to minimum of 96 mm. As shown in Table 3-1 and Table 3-2, the working distance of the Optem zoom lens (with 1X main tube) is 89 mm without any auxiliary lens and 32 mm with 2X auxiliary lens. To guarantee the proper working distance, we had to use a 0.75X auxiliary lens to increase the lens' working

distance. With the 0.75X auxiliary lens, the lens mechanism characteristics are as following (Table 3-3):

1X main tube with 0.75X auxiliary lens	**Low magnification**	**High magnification**
Magnification Range	0.39X	4.9X
Resolution	42 LP/mm	217 LP/mm
Numerical Aperture	0.014	0.072
Working Distance	114 mm	

Table 3-3: Optem zoom lens specifications with 0.75X auxiliary lens.

This lens mechanism also has a property (as opposed to other lens mechanisms), which helps us to overcome the limited working distance in the cryoimager. In this lens, at higher magnifications, we do not approach the sample but instead back away from it.

3.3.2 Camera Movement

Because of the chromatic aberration of the lens, we have different focal points for different emission wavelengths in the same image. We usually use two different wavelengths in the detection path. When we focus on one channel (e.g., the NADH channel with 445 nm), the other channel will be out of focus (i.e., the FAD channel with 520nm).

In order to eliminate this problem, we used Optem zoom lens for Cryo-microscopy. This lens is an achromatic lens system with a very small focal shift. The lens mechanism has a long tube, meaning the focal length is increased to reduce the focal shift, which results in less aberration. Although this lens is sold under the aberration free tag, it still has chromatic aberration.

Figure 3.6 shows the images of one slice of a control mouse eye (the lens of the eye is taken out to avoid saturation) in NADH, FAD, and bright field channels taken by the zoom lens. The number of girds in the grid image of the figure determines that the images are taken in microscopy. The small size of the mouse eye allows us to image the whole tissue in one field of view. Because of the focal shift error (due to chromatic aberration) of the lens, there is a compromise between the focal points of the NADH and FAD channels. This means the focus point is chosen somewhere in between each channel's focal point. Thus, both channels are out of focus and a bit blurry. The bright field channel, which uses white light illumination with no filters in either excitation or emission path, has the worst image quality.

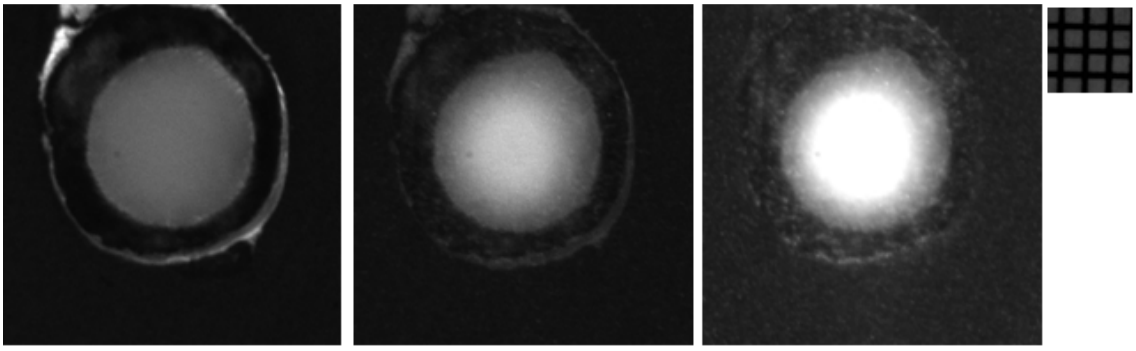

Figure 3.6: Chromatic aberration in Optem zoom, mouse eye sample.

Left) FAD channel. Middle) NADH channel. Right) Bright field channel. All images suffer from CA.

Figure 3.7 shows another mouse eye sample image taken by the Optem zoom lens in cryo-microscopy with the FAD channel in focus. It is clear that the NADH channel is out of focus.

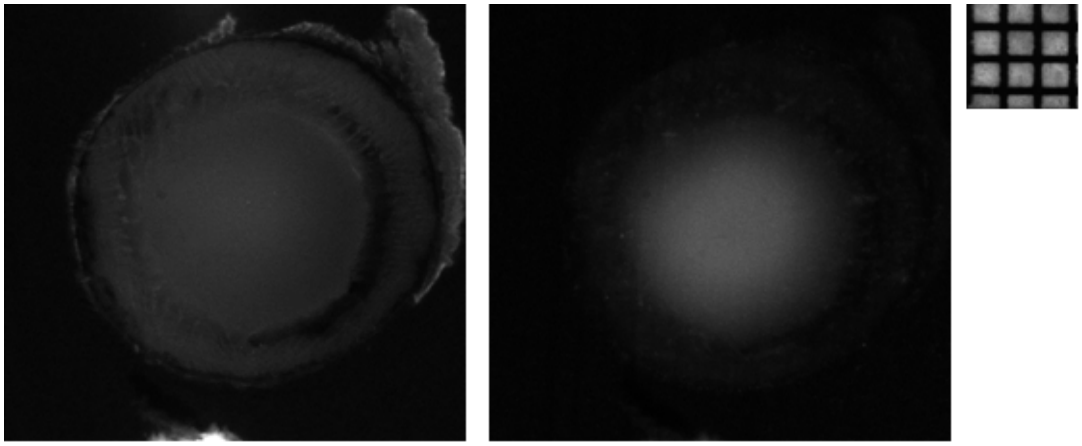

Figure 3.7: Chromatic aberration in Optem zoom lens, rat eye sample.

Left) FAD channel. Right) NADH channel. While FAD channel is in focus, NADH channel is out of focus.

The focal shift charts obtained from the manufacturer at the minimum and maximum magnification without any auxiliary lens shown in Figure 3.8 and Figure 3.9. From Figure 3.8, it can be seen that at the lowest magnification (0.55X), the maximum focal shift in the visible light spectrum is 145.5001 μm, while the shift between the wavelengths of FAD and NADH channel is 100 μm (0.1 mm). In Figure 3.9, we can see that at maximum magnification (6.9X), the maximum focal shift in visible light spectrum is 4039.6748 μm, while the shift between the wavelengths of FAD and NADH channel is 2700 μm (2.7 mm).

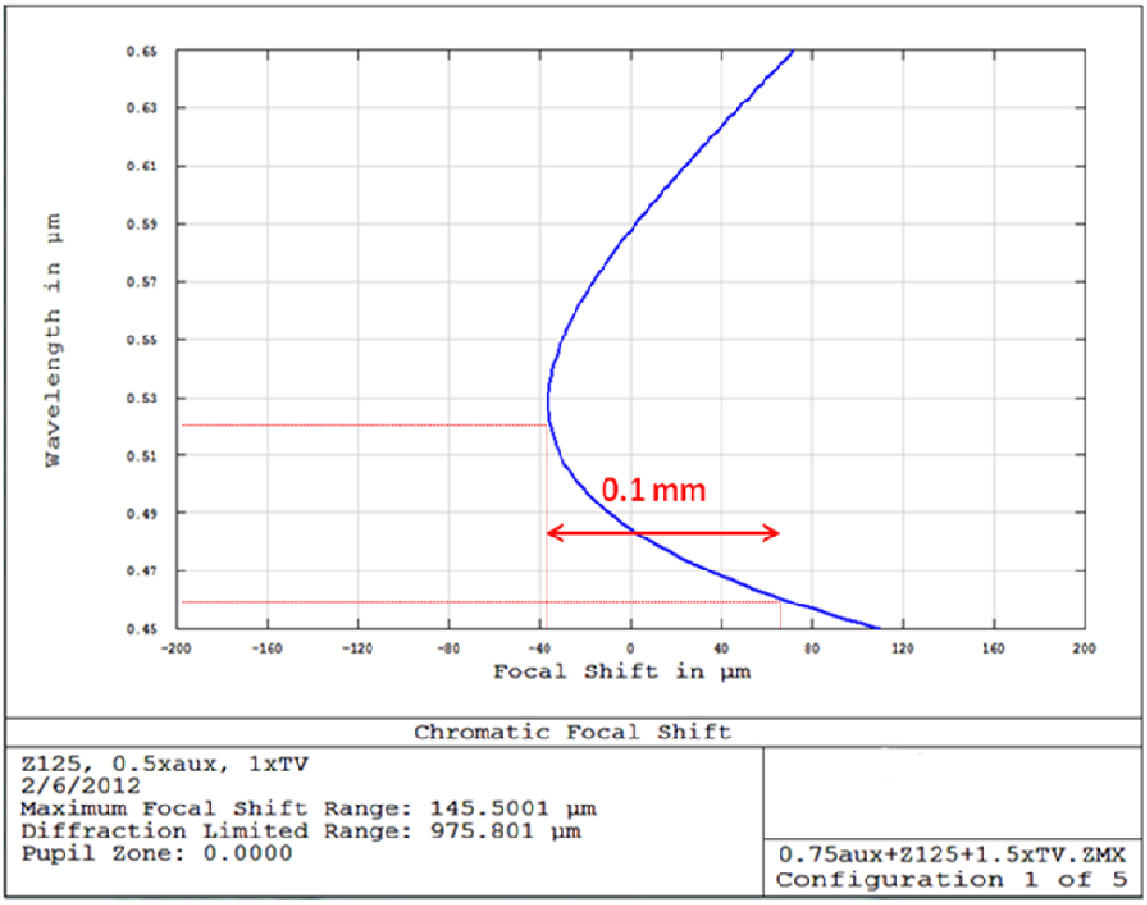

Figure 3.8: Chromatic focal shift of Optem zoom lens at 0.55X.

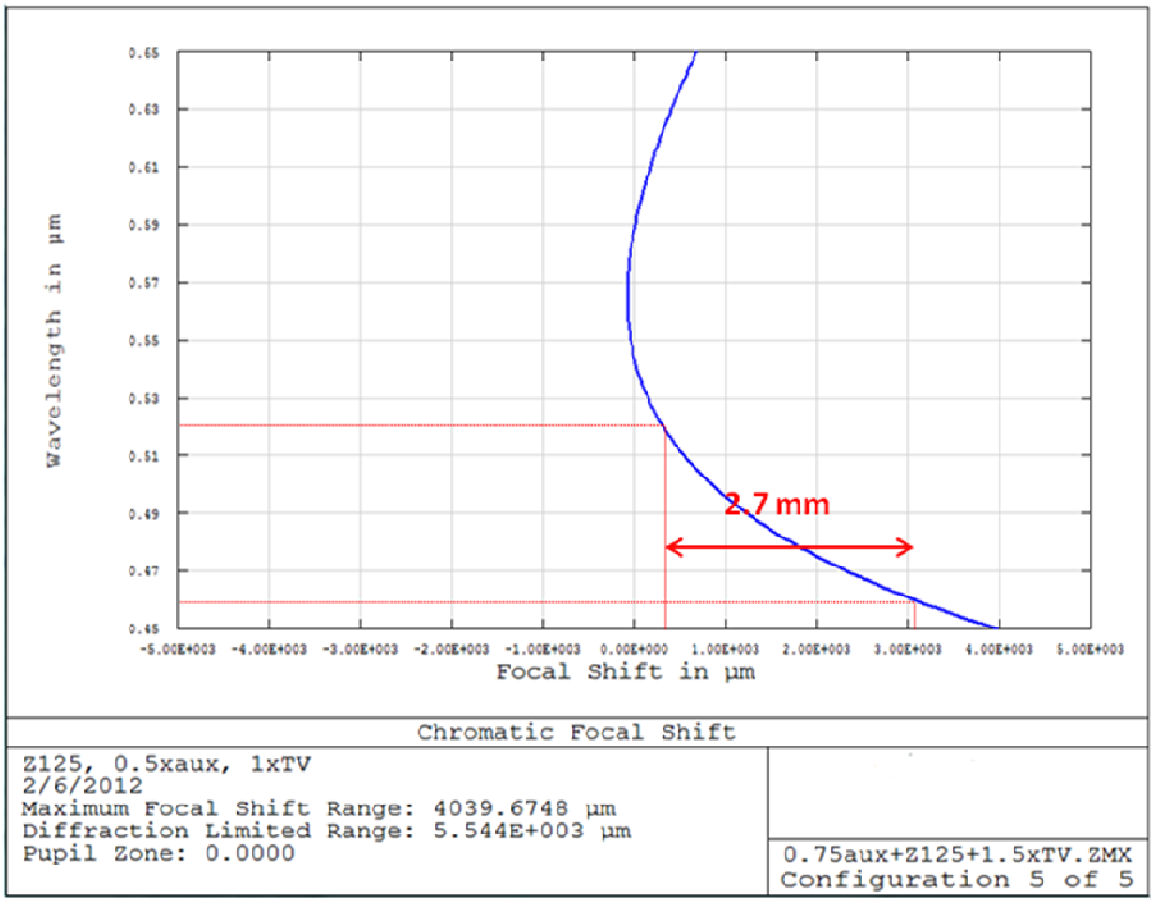

Figure 3.9: Chromatic focal shift of Optem zoom lens at 0.6.9X.

To eliminate the chromatic aberration and improve the image quality, we move the camera and lens to the focal point of the wavelength of each channel separately. To implement this plan, we used a moving stage (NRT 150, Thorlabs with 150mm moving distance) and modified the cryo-software. The stage has incremental movement of 0.1 µm with a repeatability of 1 µm and the absolute on-axis accuracy according to the manufacture is 19.29 µm. The lens and the camera are mounted on the stage, and with the help of the stage we first focus on one channel, save the position of the camera and lens, then find the focal point in the other channel and save the position of the camera and lens

in this channel as well. During the experiment, the software automatically moves the camera and lens to the appropriate focal point for each channel. Figure 3.10 shows the implementation used for both the macroscopy and microscopy setup.

Figure 3.10: Macroscopy and Microscopy setups with moving stage for camera and lens.

Top) Macroscopy. Bottom) Microscopy.

The distance that the camera and lens should move between the two channels' focal points could be calculated based on the focal shift graphs at different magnifications; in practice, however, we find it easier to determine the focal shift empirically for each experiment.

The red area in Figure 3.11 shows the changes in the software implementation necessary to control for aberration. Figure 3.12 shows the slicing, stage movements and imaging sequence after the new implementation.

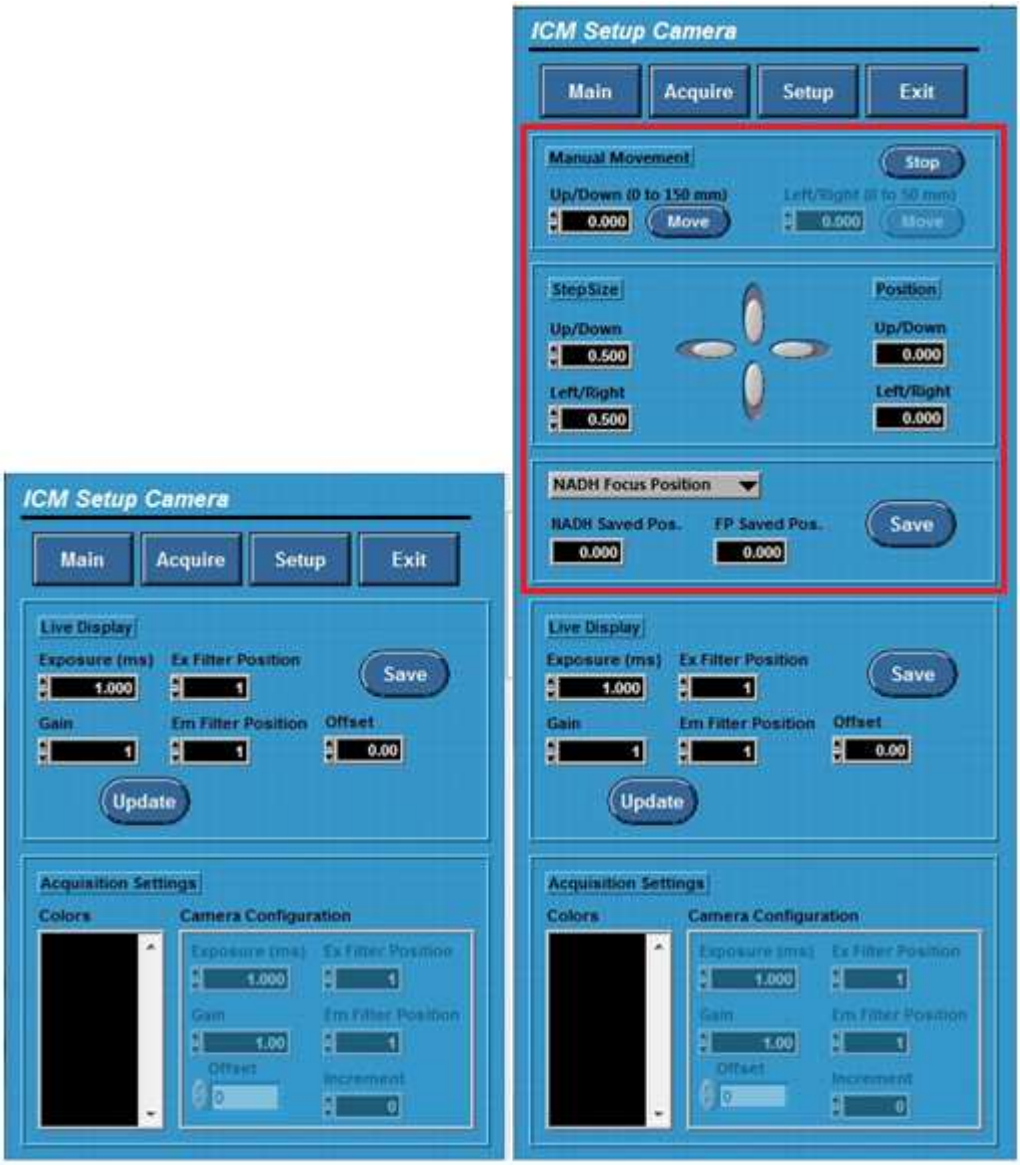

Figure 3.11: Camera setting page of the cryoimager software.

Left) Old implementation. Right) New implementation. In the new implementation, camera position can be controlled via the software.

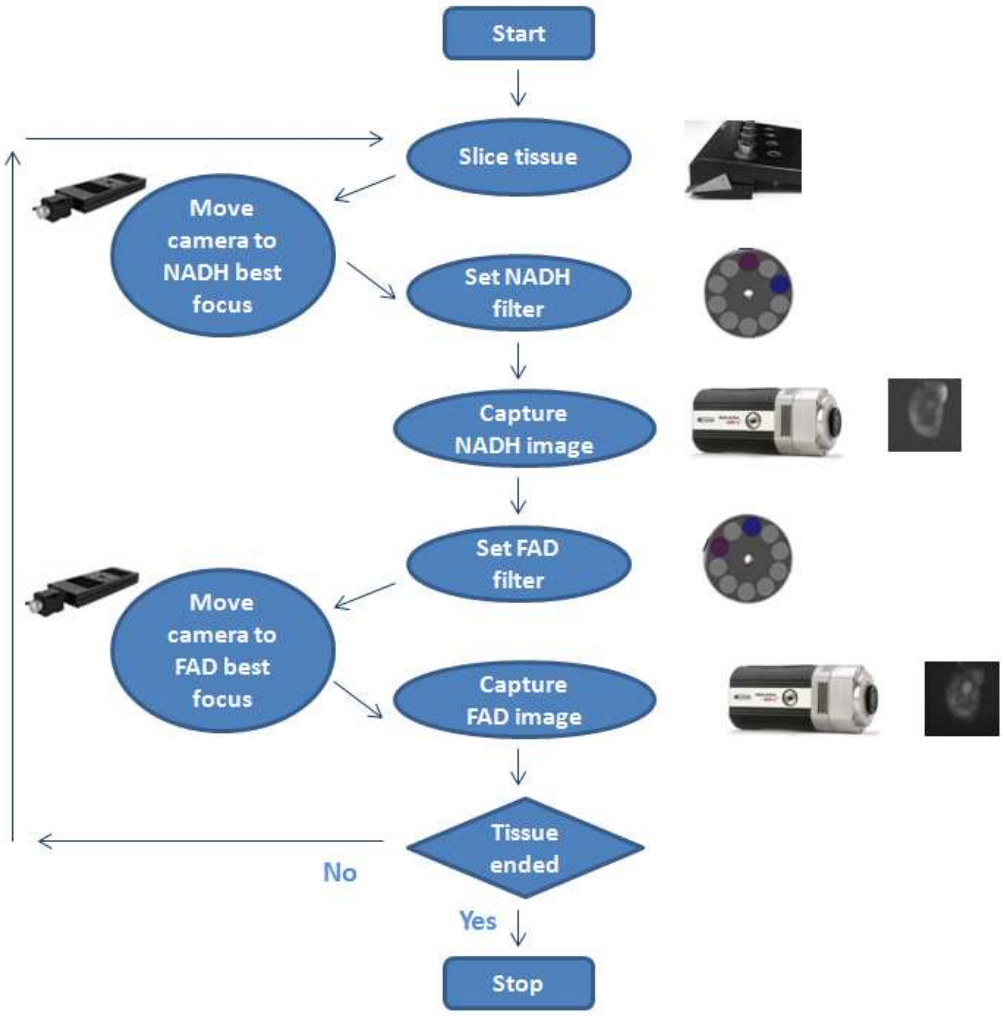

Figure 3.12: Cryoimager slicing and imaging sequence while using the moving stage.

By implementing this method, our images improved significantly and the aberration problem was solved. Figure 3.13 and Figure 3.14 show sample images taken by Canon and Optem zoom lens in both FAD and NADH channel after aberration correction, respectively. The number of grids in the gird image of each figure show that Figure 3.13 is in cryo-macroscopy and Figure 3.14 is in cryo-microscopy. After the

aberration correction, the images taken in both channels are in focus in both cryo-macroscopy and cryo-microscopy.

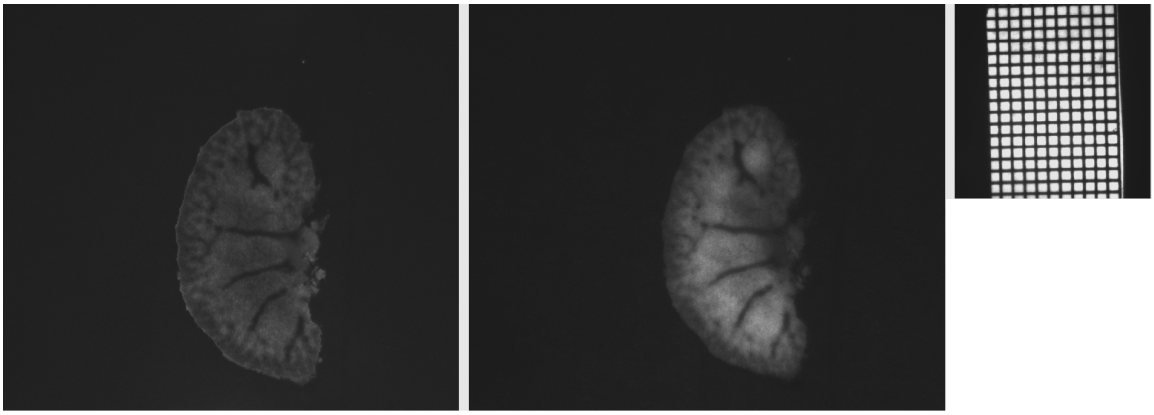

Figure 3.13: Chromatic aberration correction of rat kidney sample imaged by Canon lens.

Left) FAD channel. Right) NADH channel. Both channels are in focus.

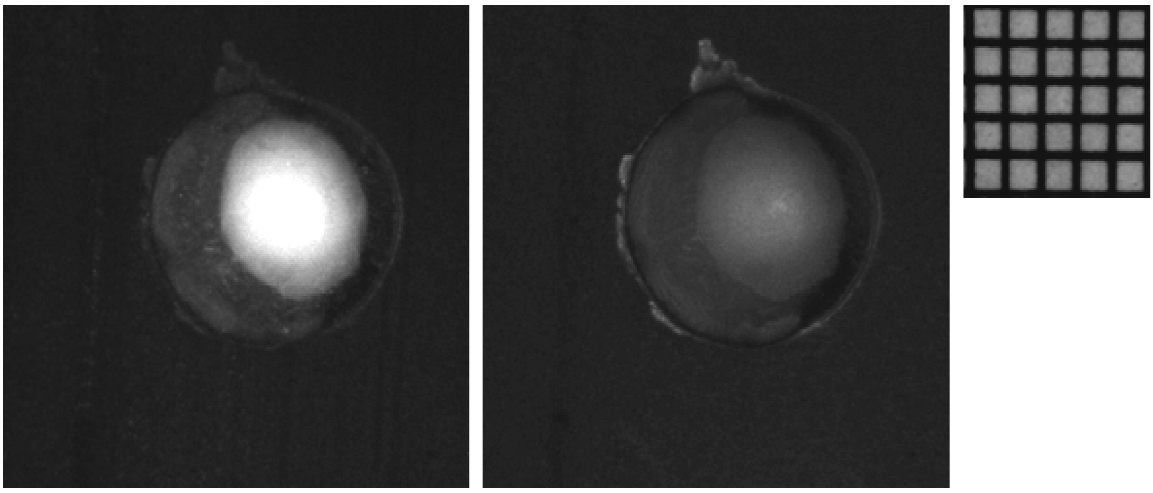

Figure 3.14: Chromatic aberration correction of mouse eye sample imaged by Optem lens.

Left) FAD channel. Right) NADH channel. Both channels are in focus.

3.3.3 Raster Scanning and Image Stitching

When magnifying the image the field of view decreases, which means the whole tissue cannot be imaged once at time for larger samples. Raster scanning is a solution to this problem. Raster scanning is implemented by subdividing the image into different fields of view, then taking images of each single field of view. These single images will be stitched together to construct the whole image. For raster scanning, movements in two directions (X and Y) are required. To implement raster scanning we have used a two-axis motorized micro stage (Standa 8MTF - Motorized XY Scanning Stage). The stage is installed vertically in the cryo freezer chamber and the tissue block is mounted onto it. This stage has movement resolution of 2.5 µm in full step and 0.31 µm in 1/8 step and can tolerate up to 6 KG load capacity in the vertical direction. This capacity is enough for the tissue block weight with allowance for the force applied to the tissue and stage from the strikes of the blade. Figure 3.15 shows the stage and how it is installed inside the cryoimager with the sample block mounted to it.

Figure 3.15: XY-stage used for raster scanning.

The raster scanning algorithm also is implemented in the cryoimager software. The red area in Figure 3.16 shows the implementation of the software.

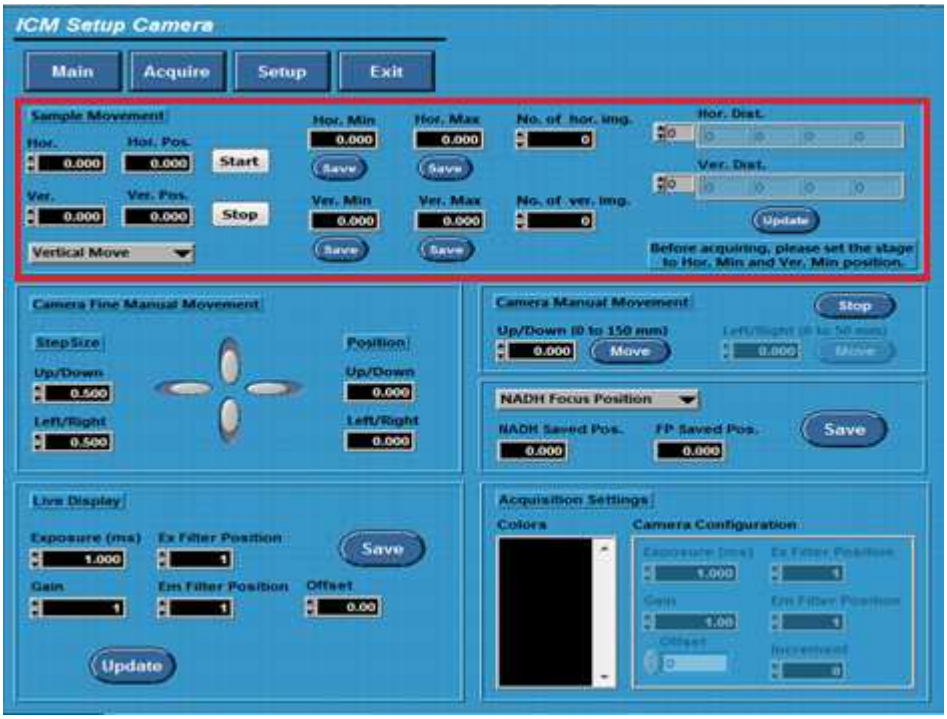

Figure 3.16: Raster scanning software implementation.

For raster scanning we need to define the tissue boundary first. This boundary can be recognized by the help of four markers (e.g., toothpicks) around the tissue when embedding the tissue in black mounting medium. By moving the stage to the positions of these markers, the four corners of our final rectangular surface are defined and saved in the software.

The number of images per slice should also be defined in the software. This number is calculated based on how big the tissue is and how magnified we want the tissue image to be. These numbers vary for the vertical and horizontal axes. By entering

the boundary positions and desired number of images into the software, the software is able to automatically calculate and save the distribution of the positions where the stage should move. The more magnification, the more images should be defined to cover the whole tissue surface (due to limited CCD camera field of view). When calculating the number of images, a safe overlap (typically %20 to %25) between the images should also be taken into consideration.

The software is implemented such that raster scanning starts from the top right-hand side of the sample and works its way down, meaning the stage should initially be positioned as far left and as low possible. Figure 3.17 shows the implemented raster scanning algorithm.

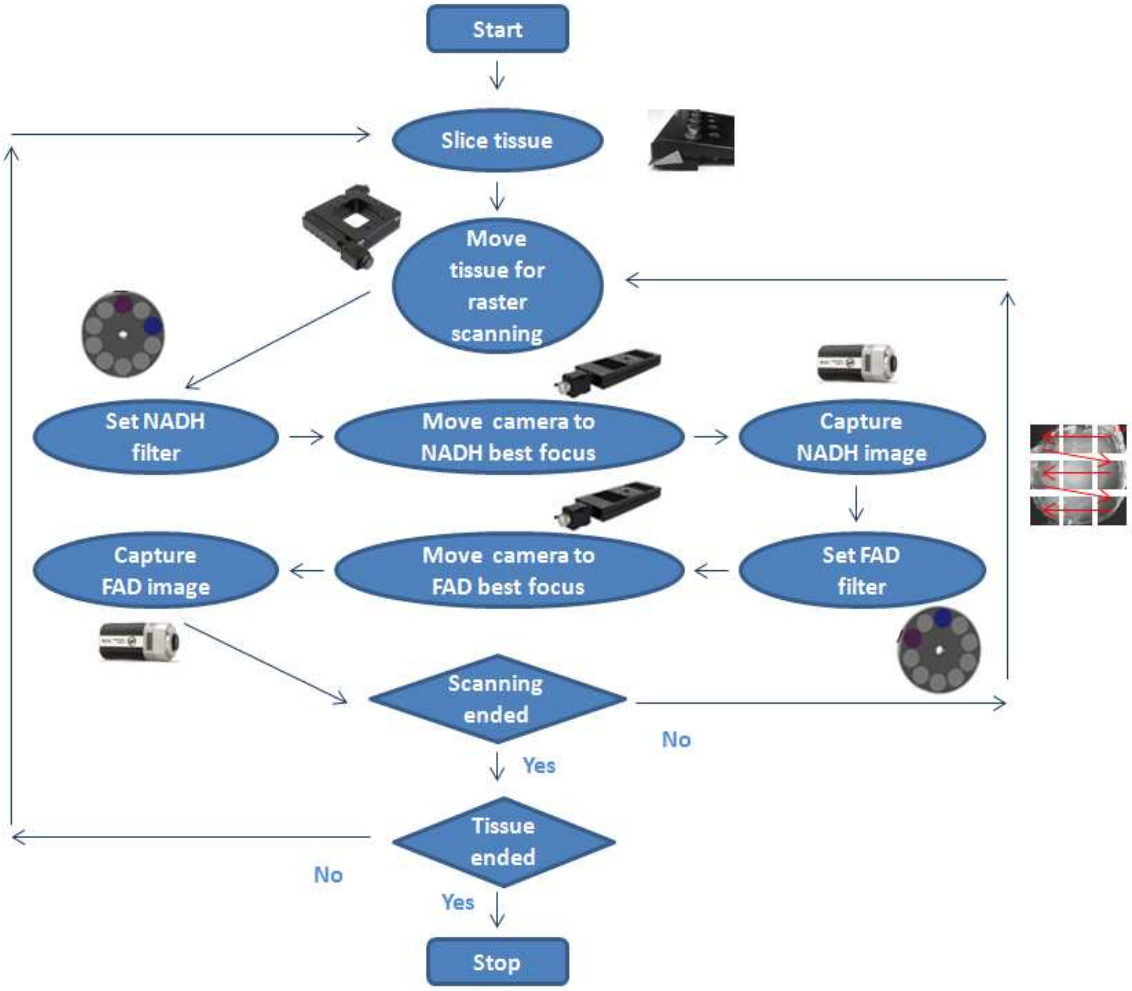

Figure 3.17: Cryoimager slicing and imaging sequence after using both stages.

Figure 3.18 shows each field of view of one slice of a control rat kidney in the FAD channel, which will be stitched to construct the image of that slice, as shown in Figure 3.19.

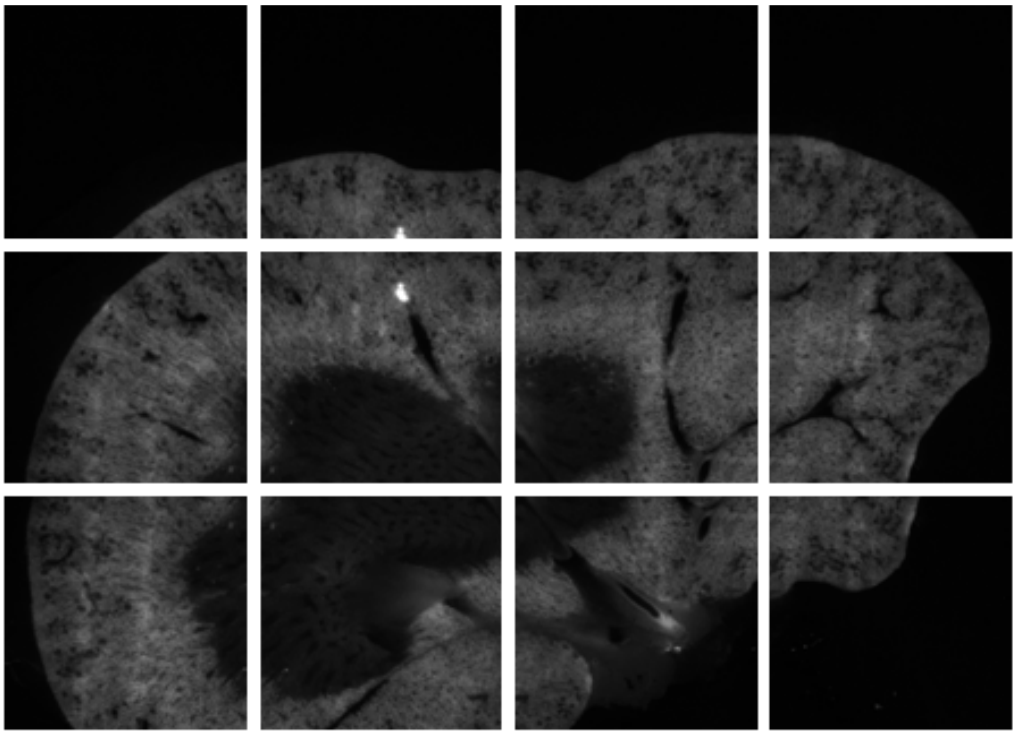

Figure 3.18: Multiple fields of view of one slice of a rat kidney sample with cryo-microscopy setup.

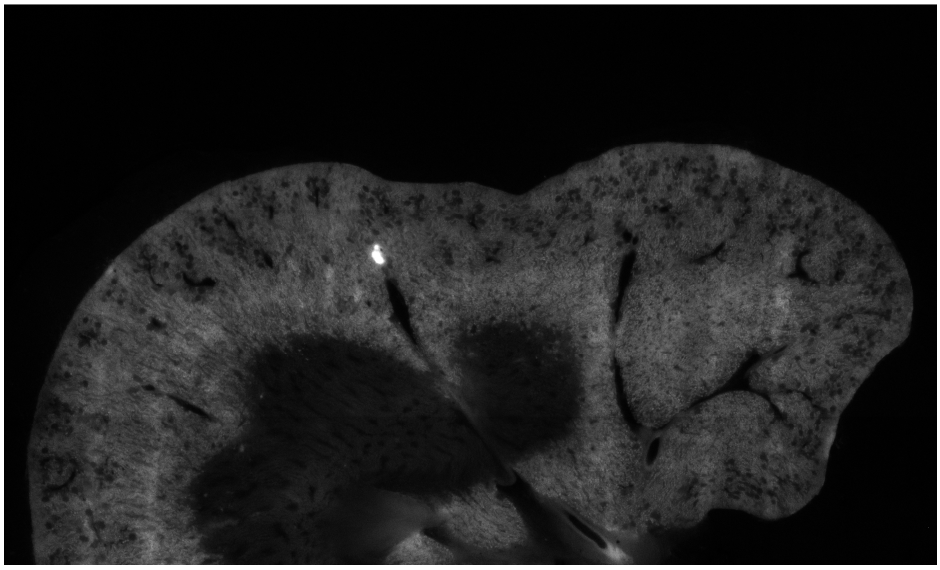

Figure 3.19: Stitched fields of view of one slice of a rat kidney sample.

Figure 3.20 and Figure 3.21 shows some selected stitched images of different layers of control rat kidneys in both macoscopy and microscopy, respectively.

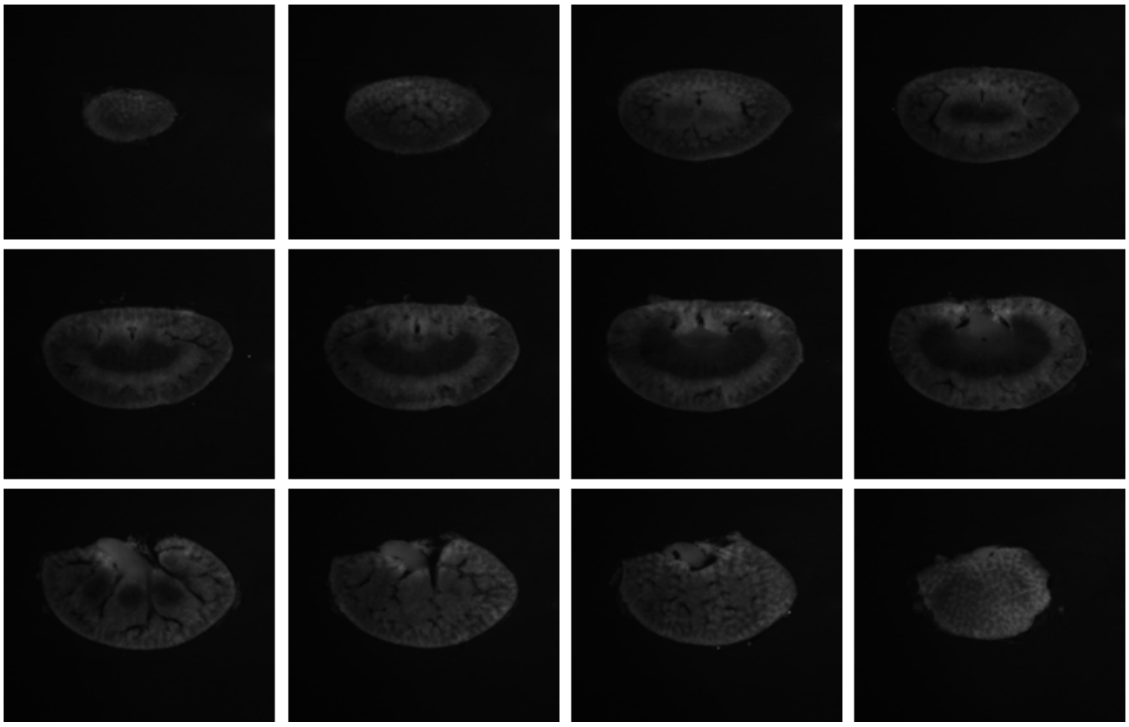

Figure 3.20: Selected images of different layers of a rat kidney sample after cryo-macroscopy.

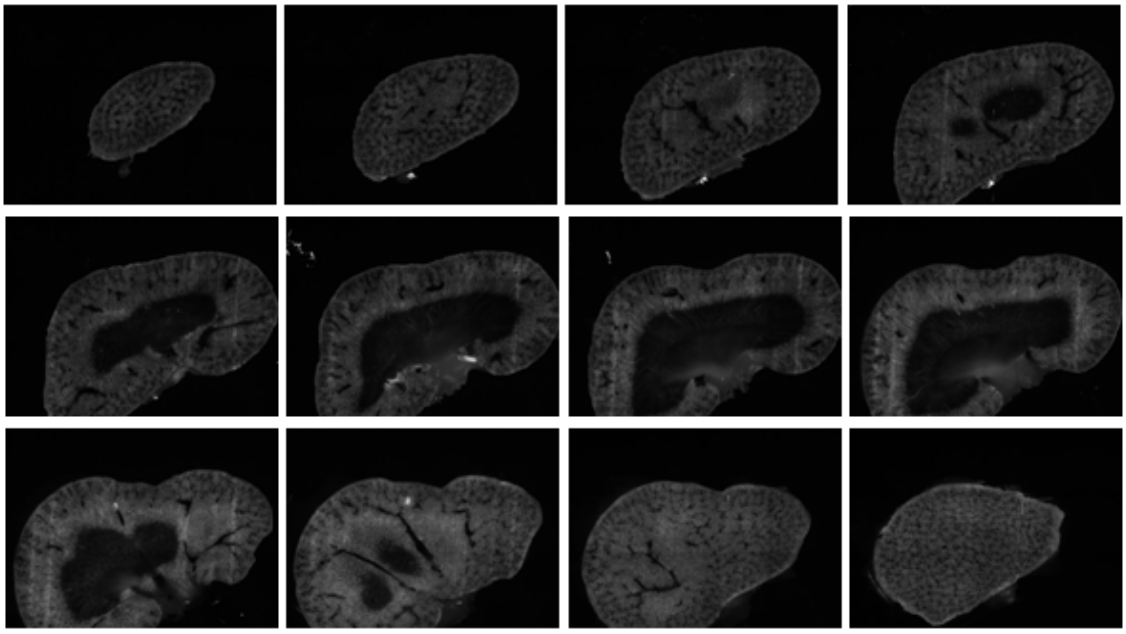

Figure 3.21: Selected images of different layers of a rat kidney sample after cryo-microscopy.

The macroscopy-imaged kidney was imaged in 300 slices with 30 μm thickness and the microscopy-imaged kidney was imaged in 60 slices with 200 μm thickness. In microscopy imaging, each slice was imaged in 12 fields of view (3*4). It is quite clear that the structures of the microscopy-imaged kidney are more recognizable and can be analyzed more easily. With the stack of the stitched high-resolution images, we are able to make 3D pictures of the tissue for both redox and structural analysis. More details about image stitching and the stitching algorithm, will be discussed in the next section.

3.4 Cryo-Microscopy Imaging Improvements

3.4.1 Images Stitching Challenges

Image stitching technique combines multiple images to produce one image, and is typically used to construct a high-resolution image. To obtain a seamless image with no artifacts after stitching, the two following conditions should be met while imaging:

1) The sub-images should be exposed to uniform homogenous illumination.

2) There should be nearly exact overlaps between the sub-images.

Figure 3.22 shows a rat eye image with severe artifacts. These artifacts between sub-images after stitching are due to light non-homogeneity. Figure 3.23 shows the illumination pattern of an individual field of view taken from a flat-field standard in the FAD channel with camera exposure of 500 ms and gain of 1. The small yellow rectangle defines one of regions where the average intensity was calculated. As shown in the

image, the five different regions have different intensity averages, which shows the light is not homogenous.

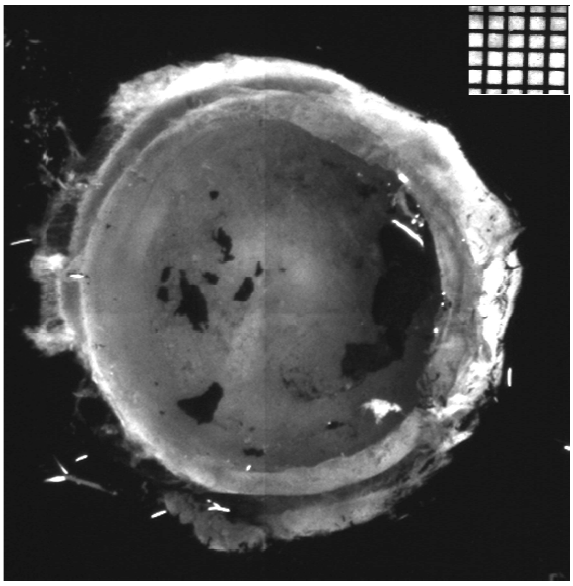

Figure 3.22: Control rat eye imaged in 4 fields of view (2*2) and stitched before light correction.

The artifacts are visible due to non-homogeneity illumination.

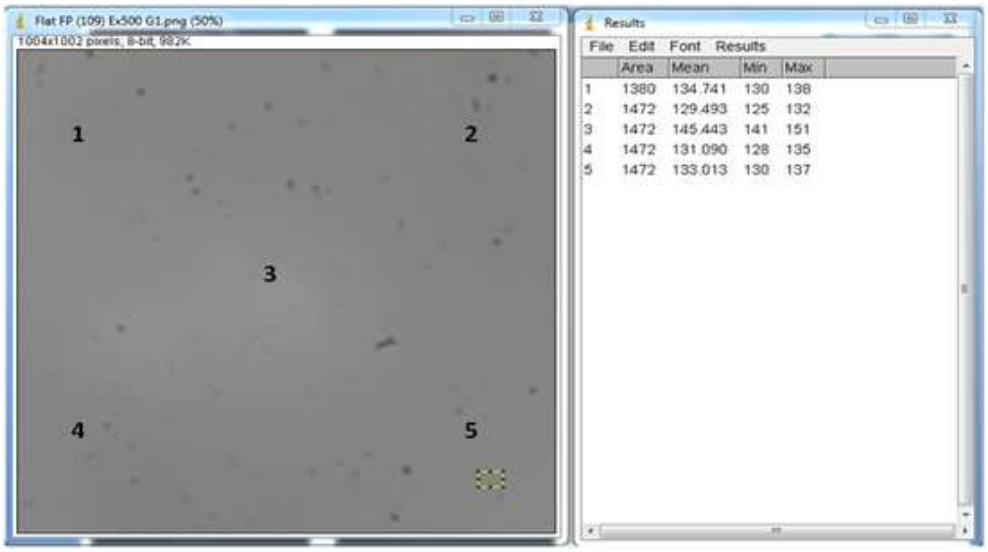

Figure 3.23: Calibration image for the control rat eye in FAD channel before light correction.

Different mean values of intensity at different regions of the flat field are showing the non-homogeneity of the illumination which causes the artifacts.

3.4.2 Solutions to Images Stitching Challenges

The illumination correction usually is done by adjusting the knobs on the mercury arc lamp. Using neutral density (ND) filters in the excitation path also helps make the light homogenous, but reduces the intensity of the light incident on the sample, which results in longer exposure times. Figure 3.24 shows the flat field illumination pattern of the same slice of the eye after the correction with shifting the knobs of the mercury arc lamp. As seen, the average intensities of different regions are closer, which results in a smoother stitched image. Figure 3.25 shows the eye slice after illumination pattern correction. As seen, the artifacts are almost entirely eliminated.

Overlapping problem is also solved in the implemented stitching software and will be explained in the following section.

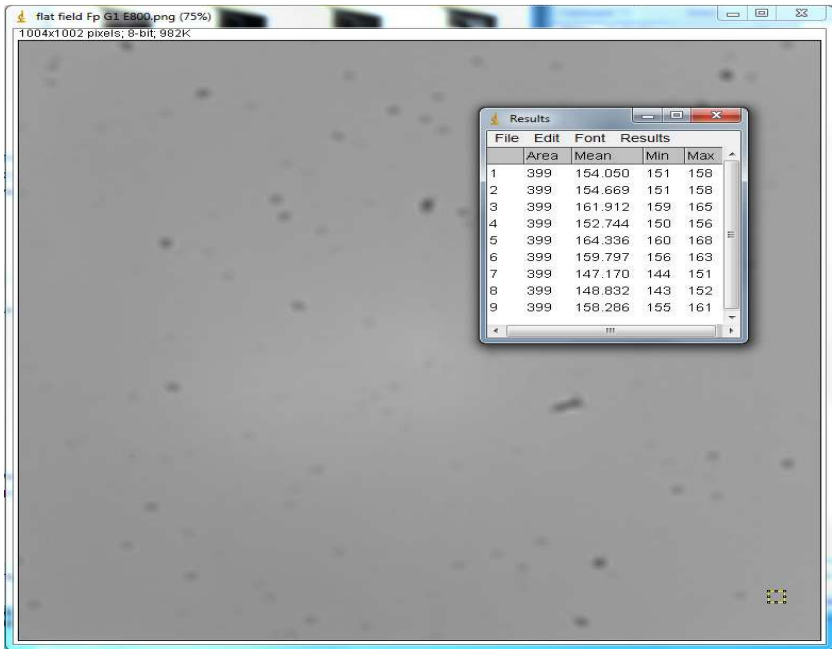

Figure 3.24: Calibration image for the control rat eye in FAD channel after light correction.

Average intensities at different regions of the flat field are closer which results in smoother image.

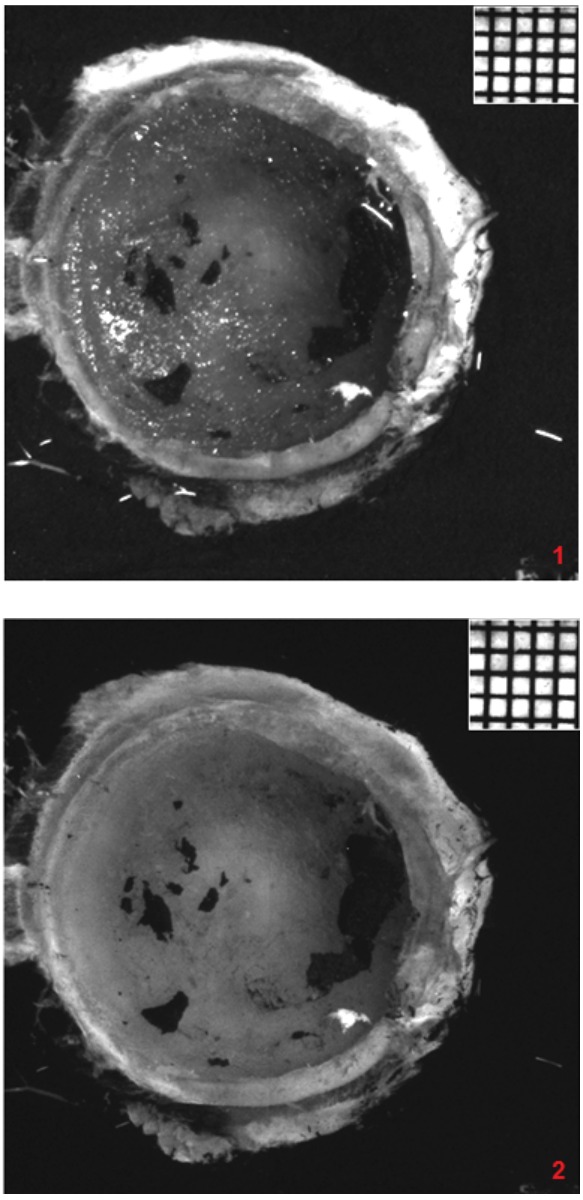

Figure 3.25: Control rat eye imaged in 4 fields of view (2*2) and stitched after light correction.

1) NADH channel 2) FAD channel. The artifacts are eliminated.

3.4.3 Images Stitching Software

A user-friendly software is implemented in LabVIEW for automated image stitching. Figure 3.26 shows the software panel and the parameters needed for fine stitching.

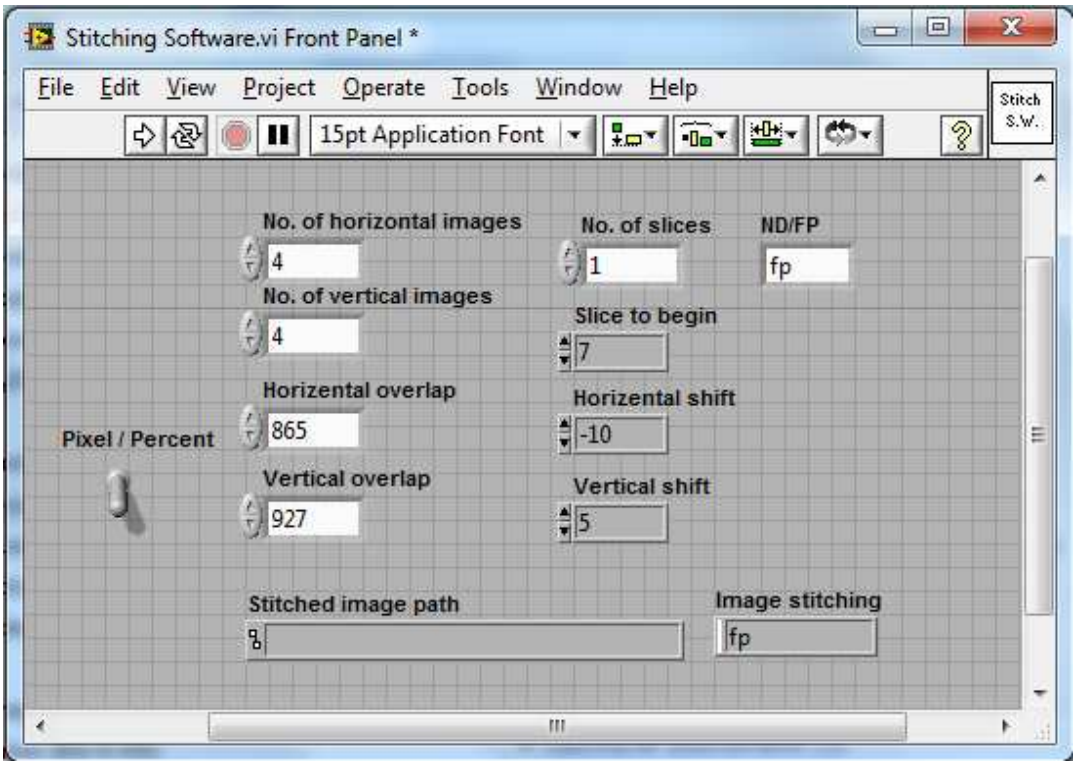

Figure 3.26: The automatic stitching software implemented in LabVIEW.

The software is able to eliminate the imprecise movements of the stage.

In the software panel, the number of images (fields of view) per slice should be defined. These numbers are exactly the same as those defined when the tissue was imaged. The overlap between images can be defined in both percentage and number; the pixel/percent switch allows the user to toggle between the two.

The software requires other parameters such as the total number of slices, which slice to begin stitching, and in which channel (NADH or FAD) the images were acquired

Artifacts are not always due to the illumination. Since the step movements of the stage are not precise, after stitching the artifacts would appear.

This software has also the ability to remove the artifacts from the imprecise movements of the stage by shifting pixels positions' when stitching. Figure 3.27 shows the artifacts in a slice of a rat kidney made due to the imprecise movement of the stage and Figure 3.28 shows one-axis corrected image of another slice of that rat kidney.

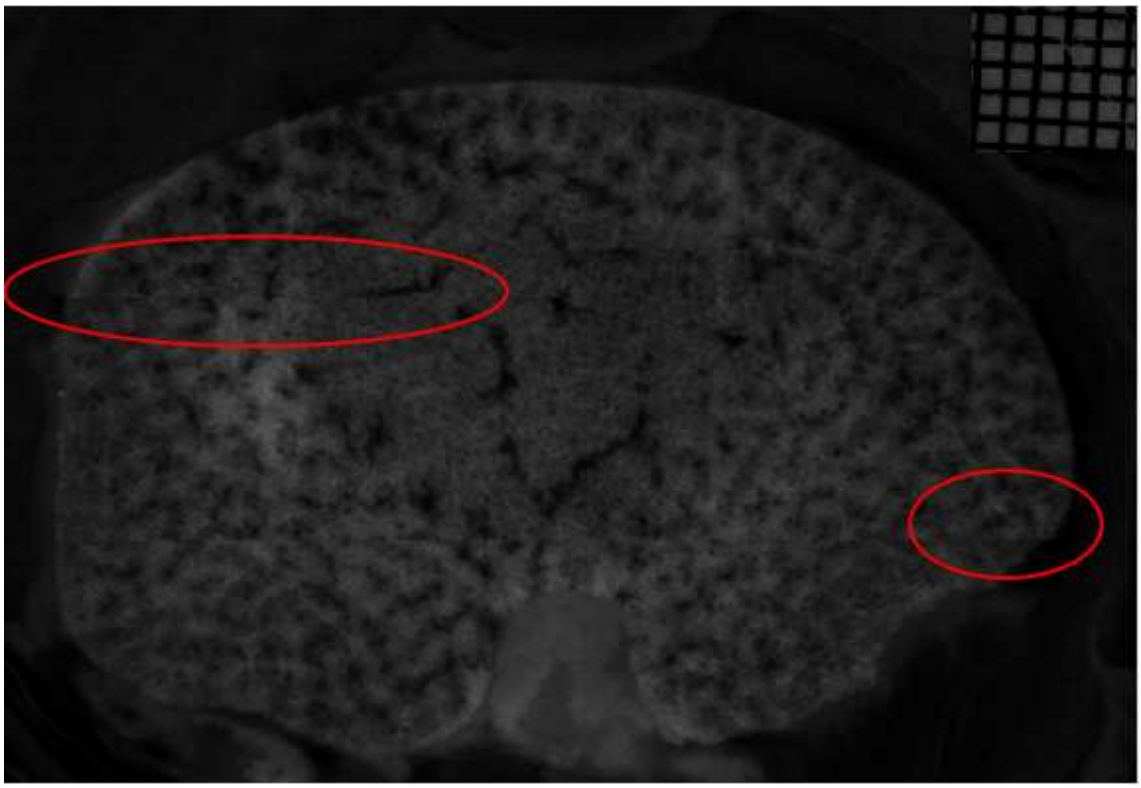

Figure 3.27: Artifacts in stitched image of a control rat kidney.

These artifacts are made because of the imprecise movement of the stage.

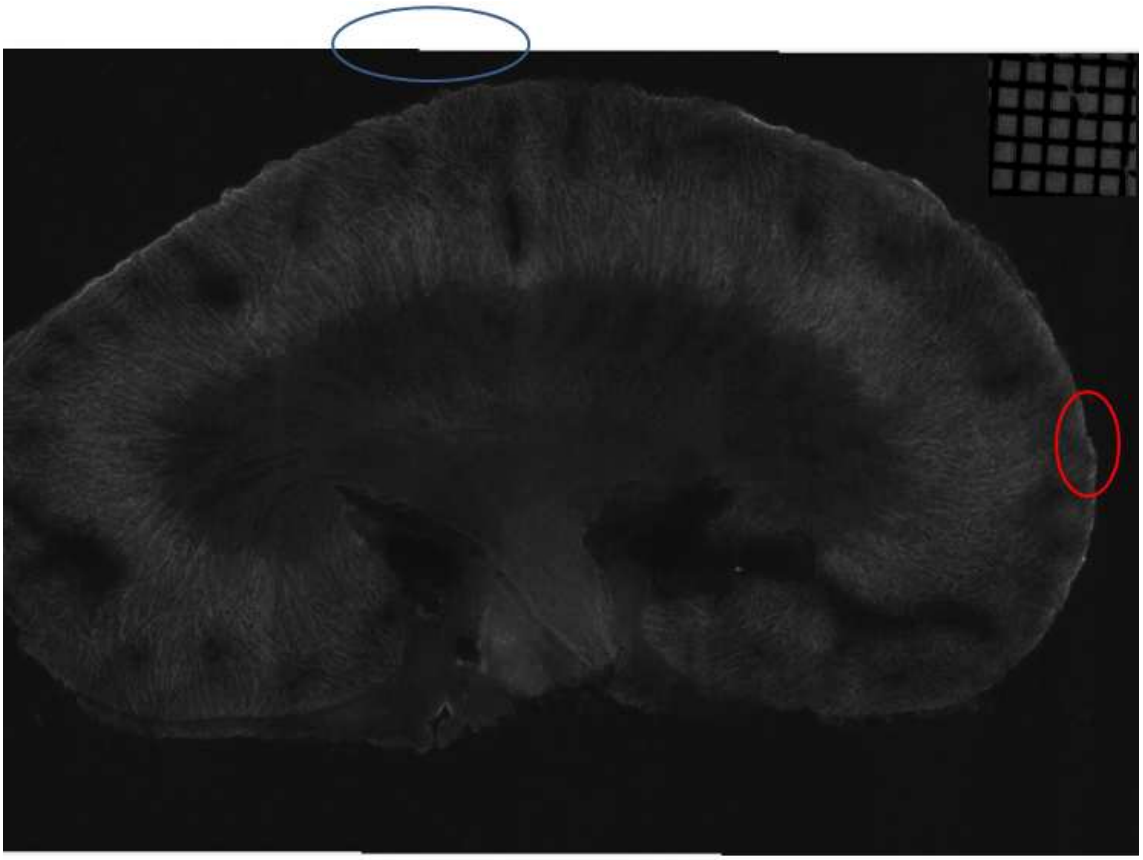

Figure 3.28: One-axis corrected stitched image.

Region in blue ellipse shows the image is corrected while region in red ellipse still suffers the artifact.

In Figure 3.28 the vertical artifacts are eliminated but the horizontal ones are still remaining because of no correction in that axis.

After obtaining corrected high resolution images in cryo-microscopy, same software and techniques explained in image processing section of chapter 2 are used to calculate the redox of the tissue samples and to make 3D panels from them.

Chapter 4

Biological Applications of

Cryo-Macroscopy and Cryo-Microscopy

4 Biological Applications of Cryo-Macroscopy and Cryo-Microscopy

4.1 Introduction

In the previous chapters, cryo-macroscopy, cryo-microscopy, and the images captured in each setup were explained. In this chapter, the biological applications of both cryo-macroscopy and cryo-microscopy are discussed.

In my research, I studied the mitochondrial redox state in bronchopulmonary-dysplasia injury models in mice lungs in macroscopy. The results obtained, validate cryoimaging method performance in measuring the oxidative state. Then I studied the structural changes in the tissue due to the diseases that change the mitochondrial redox state of the tissue. To reach this goal, I studied kidneys of animal model (Endoglin gene knock out rat), imaged them in microscopy and showed the structural changes in high resolution 3D rendering while the tissue redox state is monitored at the same time.

4.2 Cryo-Macroscopy Imaging: Bcl-2 (BPD model)

Bronchopulmonary dysplasia (BPD) is a chronic lung condition that affects premature infants who receive supplemental oxygen (hyperoxia) or ventilator support for long periods of time. Studies have shown that arrest of alveolar development is a

hallmark of BPD caused by either oxygen or mechanical ventilation. We have observed significant abnormalities in lungs prepared from Bcl-2 null mice perhaps as a result of increased oxidative stress and reduced angiogenesis [43]. Our hypothesis is that oxidative stress plays a key role in development of vascular dysfunction associated with BPD. We used optical cryo-imaging to investigate the mitochondrial redox state of the tissue related to oxidative stress and pathogenesis of BPD. Here we tested whether deficiency in Bcl-2, an anti-apoptotic protein with important role in angioegenesis, results in increased oxidative stress (OS) and attenuation of lung angiogenesis contributing to PBD.

In this research lungs from three groups of mice were studied: Bcl-2 +/+, Bcl-2 -/- (global Bcl-2 null) and Bcl-2 VE-cad (Bcl-2 only deleted in the endothelium). Bcl-2 +/+ lungs were used as control and Bcl-2 VE-cad and Bcl-2 -/- mice were used as potential models of BPD. The mice were sacrificed at 3 weeks of age.

Bcl-2 family acts as regulators of oxidative stress that affect the metabolic state of the tissue. Absence of Bcl-2 causes a more oxidized state in tissue and, as such, the mitochondria are more oxidized in Bcl-2 -/- mice as compared with their controls.

The results are shown in Figure 4.1. Figure 4.1 (left) shows the 3-D rendering of NADH and FAD fluorescence signals and their ratio (RR = NADH/FAD) from representative lungs of each of the three groups (Bcl-2 VE-cad vs. Bcl-2 +/+ on top and Bcl-2 -/- vs. Bcl-2 +/+ on bottom). As expected, mice with global Bcl-2 null and Bcl-2 VE-cad show a decreased NADH signal and increased FAD signal and as a result decreased RR in respect to the control mice (26% decrease for Bcl-2 VE-cad and 47% for

Bcl-2 -/-) which implies generation of more ROS and oxidative stress. Bcl-2 -/- mice also had more ROS and oxidative stress (OS) compared with Bcl-2 VE-cad.

Figure 4.1 (right) shows histograms of RR for the lungs. The mean values of these histograms suggest a more reduced mitochondrial redox state for Bcl-2 +/+ lung, and more oxidized mitochondrial redox state for both Bcl-2 VE-cad and Bcl-2 -/-.

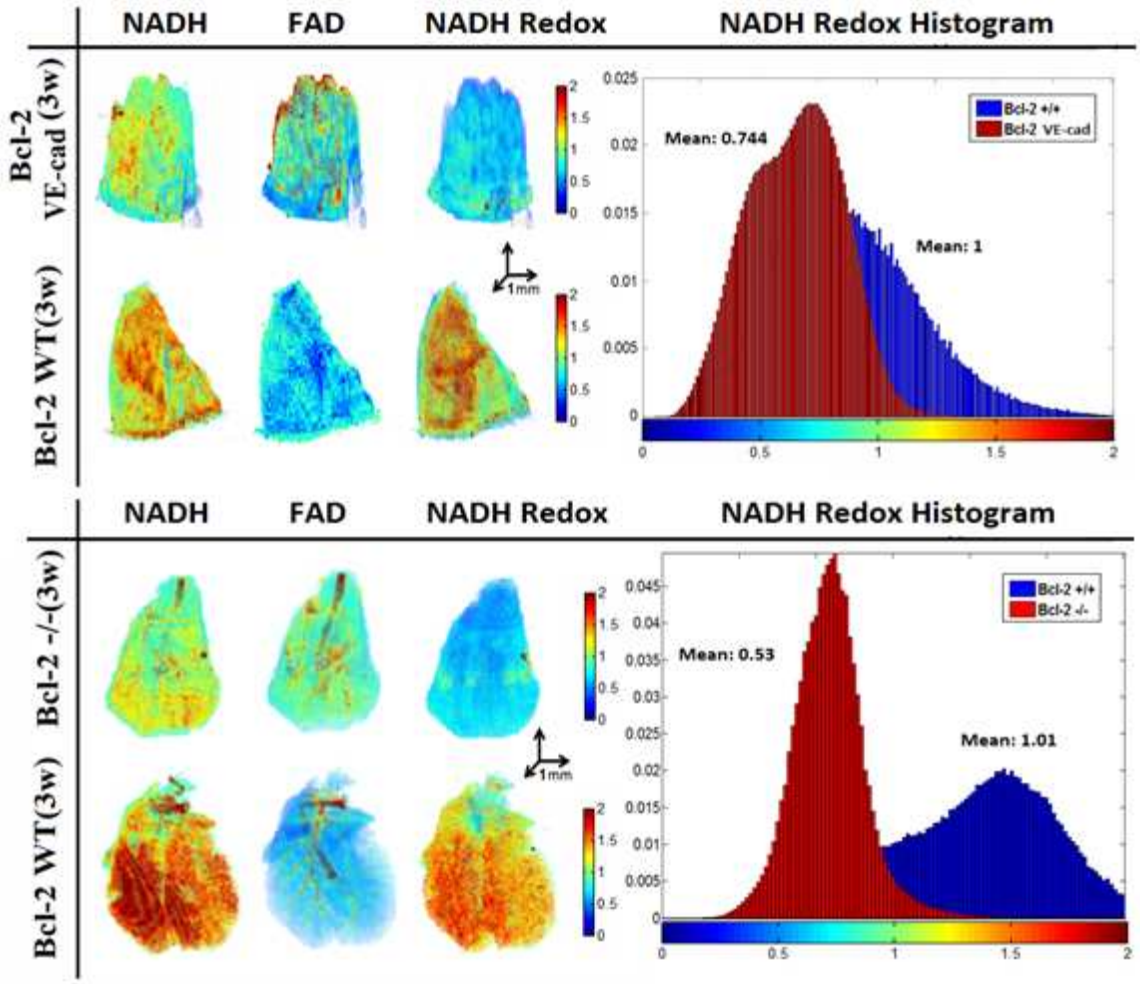

Figure 4.1: Fluorescence images and histograms of Bcl-2 mouse lung.

Left) Fluorescence images of from left to right NADH, FAD and NADH redox in a Bcl-2 VE-cad vs. Bcl-2 +/+ mouse lung on top and Bcl-2 -/- vs. Bcl-2 +/+ on the bottom. Right) Histogram of control (blue) and Bcl-2 VE-cad lung (red) on top and control (blue) and Bcl-2 -/- lung (red) on bottom.

Figure 4.2 Figure 1 (c) shows the average ±SE (standard errors) of the mean values of the redox ratio histograms for the three groups of mice, which shows a significant decrease ($p<0.021$) in the NADH redox in Bcl-2 VE-cad lungs and Bcl-2 -/-.

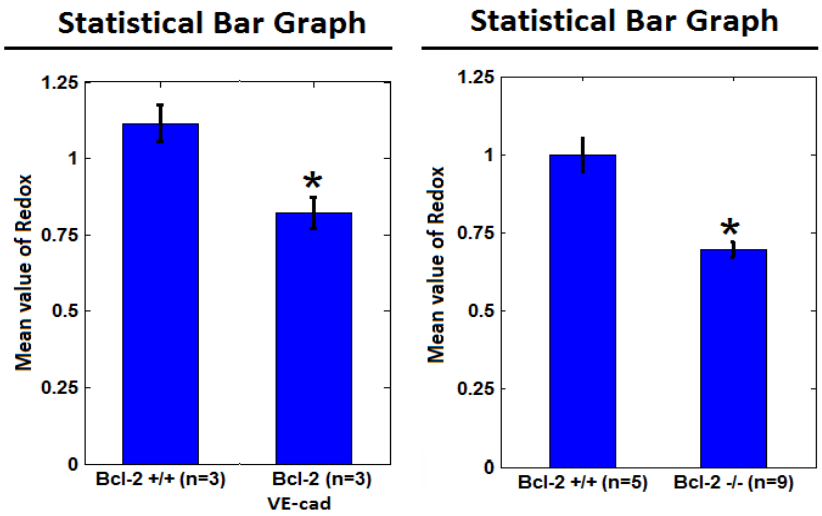

Figure 4.2: Mean value bar graph of mitochondrial redox ratio.

Bar graph showing the means and standard errors of the mean value of mitochondrial redox ratio ($p<0.021$) Left) Control and Bcl-2 VE-cad. Right) Control and Bcl-2 -/-.

The utility of cryoimaging for evaluating the redox status of tissue mitochondrial coenzymes NADH and FAD was previously shown in intact lungs in another model of BPD (combining injuries due to ventilation with elevated oxygen concentration and bacterial infection) [44]. It was illustrated that the redox ratio (RR), NADH/FAD, is an index of lung tissue mitochondrial redox state, which is an important determinant of mitochondrial bioenergetics. Here we have shown that mice lacking Bcl-2 demonstrate increased oxidative stress as seen in BPD phenotype. Bcl-2 is a key mediator of downstream events that occur in response to both pro- and anti-angiogenic factors,

including VEGF and thrombospondin-1 (TSP1), respectively [45]. The important role Bcl-2 plays during angiogenesis is demonstrated by the inability of Bcl-2 -/- endothelial cells to undergo capillary morphogenesis and sprouting angiogenesis [46].

A clearer understanding of mitochondrial dysfunction and the role Bcl-2 plays in this process is critical for elucidating the role of mitochondrial bioenergetics in pulmonary developmental arrest and can be further used in prevention of BPD-like injuries. Our studies show that deficiency of Bcl-2 in the endothelium is only partially responsible for increased oxidative stress. The identity of additional cellular components to increased oxidative stress in the global null mice awaits further investigation.

Other endogenous (intrinsic) fluorophores in the tissue, including collagen and elastin, would not be expected to contribute in variations of mitochondrial redox state [47] [48]. Contribution of cytosolic NADPH, which has the same fluorescence characteristics as NADH, to the NADH fluorescent signal is considered to be small [49] since its concentration and quantum yield is much smaller than NADH [50].

4.3 Cryo-Microscopy Imaging: Endoglin (HHT-1 model)

The structure of organs and the redox ratio are both affected by disease progression. The changes in the mitochondrial redox state reflect physiological states that can be directly or indirectly related to structural changes. In order to study this correlation, we added microscopy capability to the cryoimager. We started to investigate the structural changes in the vasculature of kidneys simultaneously with redox

measurements in diseases such as HHT-1 (Hereditary hemorrhagic telangiectasia) and diabetes.

We are in a unique position to identify early points of intervention to protect kidney function during diabetes. We tested the hypothesis that the reduction in the level of metabolic state (redox ratio) is related to an increase in the level of oxidative stress occurring in the renal vasculature and proximal tubules during diabetes. These studies will establish a time frame for induction of renal oxidative stress during diabetes and its association with renal vascular and tubule dysfunctions.

HHT-1 is a good model to study the way in which a disease affects structural changes in the vasculature network of different organs. This disease is a dominant vascular dysplasia caused by loss-of-function mutations in the human Endoglin gene. HHT-1 results in excessive bleeding and vascular malformation due to failure to recruit perivascular supporting cells to the newly forming blood vessels [51].

HHT-1 is associated with frequent nose bleeds, telangiectases, mucosa, and arteriovenous malformations in lung, liver, kidney, and brain [51] [52].

Complete deletion of Endoglin is embryonically lethal. Indeed, Endoglin knockout mice (Eng -/-) die in utero from cardiovascular defects due to inappropriate remodeling of their mature vascular network [52] [53] [54] [55].

Using the cryo-microscopy setup I implemented, the vasculature in Endoglin heterozygote (Eng +/-) mice was targeted and studied. These mice show some of the same vascular defects with as humans with Endoglin haploinsufficiency [56], and therefore continuing this study can reveal some unknown aspects of this disease, which

could help to diagnose and quantify the amount of injury incident to organ by this disease. 3D cryo-microscopy optical imaging showed that vasculature network in kidney from Eng +/- mice demonstrates following properties as compared to normal mice:

- More branching
- Smaller caliber
- Smaller vessel coverage
- More tortuosity
- Premature branching

Figure 4.3 shows a maximum projection representation of NADH and FAD fluorescence signals and the NADH redox ratio from an Endoglin knockout mouse (Eng +/-) kidney versus a wild type mouse (Eng +/+) kidney, both sacrificed at 9 month of age. It can be seen that the Endoglin knockout mouse shows an increased NADH signal and decreased FAD signal and as a result increased NADH redox ratio.

Figure 4.4 shows histograms of the NADH redox ratio for the two kidneys (Eng +/- and Eng +/+). The mean values of these histograms suggest a more oxidized mitochondrial redox state for Eng +/- kidney, and more reduced mitochondrial redox state for Eng +/+.

Figure 4.5 and Figure 4.6 also show the Eng +/-and Eng +/+ mouse kidneys imaged in microscopy configuration. A 3D rendering of both kidneys illustrate more branching with smaller caliber and vessel coverage in vasculature network of an Eng +/- kidney. These vessels have more tortuosity and demonstrate premature branching in comparison with an Eng +/+ kidney which prove our hypostasis.

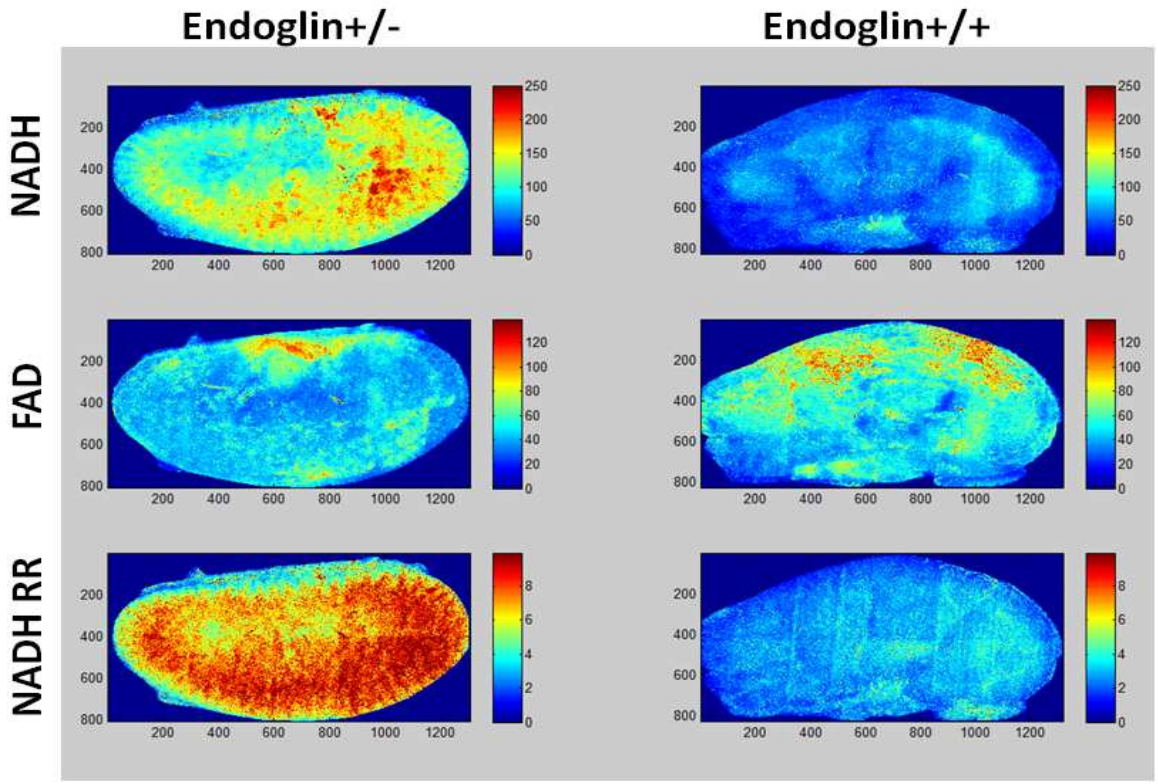

Figure 4.3: Maximum projection of NADH, FAD and NADH redox in 9 month Eng +/- and Eng +/+ mouse kidney.

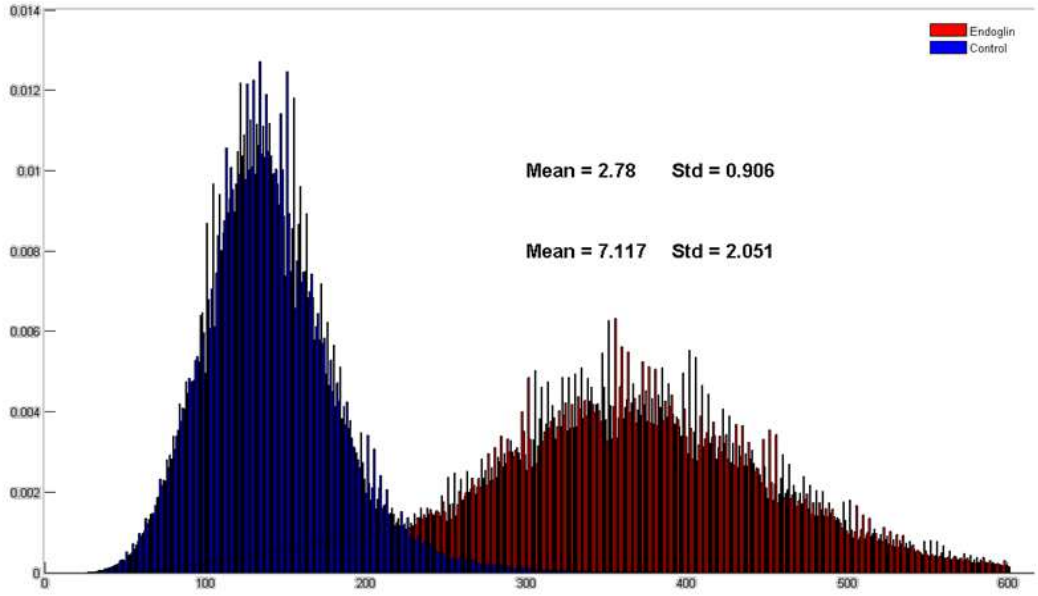

Figure 4.4: Histogram of NADH redox in 9 month Eng +/- (blue) and Eng +/+ (red) mouse kidney.

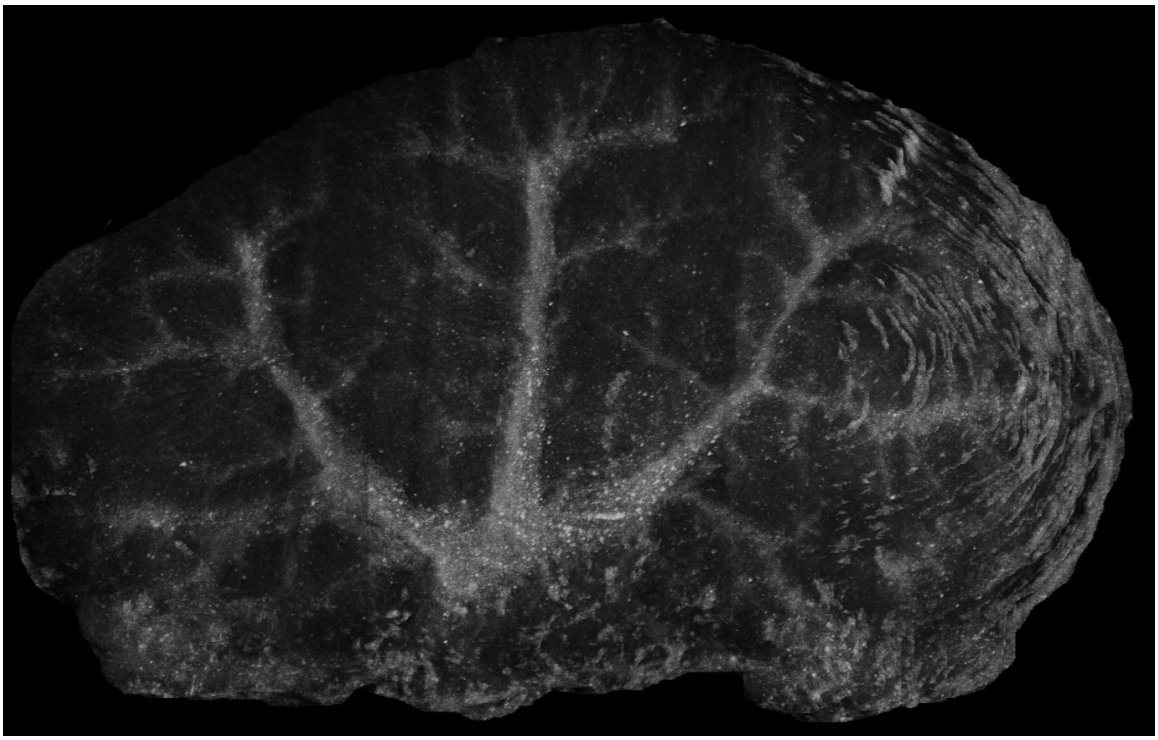

Figure 4.5: 3D rendering of NADH redox in 9 month Eng +/+ mouse kidney.

Figure 4.6: 3D rendering of NADH redox in 9 month Eng +/- mouse kidney sample.

Chapter 5

Conclusion and Future Work

5 Conclusion and Future Work

5.1 Conclusion

I designed and implemented cryo-microscopy for high resolution visualization of 3D tissue structures to monitor the amount of injury in tissue due mitochondrial dysfunction and structural damage.

I also implemented a raster scanning algorithm for capturing high resolution and magnified images. Thirdly I implemented a stitching algorithm to automatically stitch multiple raster images to obtain one high resolution image. To eliminate the artifacts on the stitched images, the illumination pattern was corrected and shifting method was employed in the stitching software to compensate the imprecise movements of the cryoimager stage in microscopy configuration.

Capturing the fluorescence images in microscopy resolution enables us not only to determine the oxidative state of the tissue, but also to visualize the tissue structure. The correlation between the changes in the mitochondrial redox state and the structural changes of the tissue is beneficial.

I studied the oxidative stress of three groups of mice lungs with 3 weeks of age. Bcl-2 +/+, Bcl-2 -/- (global Bcl-2 null) and Bcl-2 VE-cad (Bcl-2 only deleted in the endothelium). Bcl-2 +/+ lungs were used as control and Bcl-2 VE-cad and Bcl-2 -/- mice were used as potential models of chronic lung condition in premature infants named bronchopulmonary dysplasia (BPD).

We observed a 47% and 26% decrease in the NADH redox in Bcl-2 deficient lungs, Bcl-2-/- and Bcl-2 VE-cad, respectively. Thus, Bcl-2 deficiency is associated with significant increase in oxidative stress contributing to reduced angiogenesis and enhanced pathogenesis of BPD.

Using 3D cryo-microscopy setup which I implemented, I also studied the structural changes in the vasculature of rat kidneys in diseases such as HHT-1 (Hereditary hemorrhagic telangiectasia) and diabetes while measuring the tissue redox simultaneously. HHT-1 is a dominant vascular dysplasia caused by loss-of-function mutations in the human Endoglin gene and leads to diabetes.

In this research, I targeted the vasculature in 9-month old Endoglin heterozygote (Eng +/-) mice was and showed that vasculature network in kidney from Eng +/- mice have more branching, smaller caliber, smaller vessel coverage, more tortuosity and premature branching in respect to control mice.

The Endoglin knockout mouse also showed an increased NADH signal and decreased FAD signal and as a result increased NADH redox ratio. As a result Eng +/- kidney have more oxidized mitochondrial redox state and Eng +/+ kidney have more reduced mitochondrial redox state as expected.

These results can be used to identify early points of intervention to protect kidney function during diabetes.

5.2 Future Work

The mice studied in cryo-micorscopy have some of the same vascular defects as humans with Endoglin haploinsufficiency, and continuing this study can reveal some unknown aspects of this disease, which could help diagnosing and quantifying the amount of injury incident to the kidney by this disease. Especially when it is known that the reduction in redox ratio is related to an increase in the level of oxidative stress occurring in the renal vasculature and proximal tubules during diabetes.

The next step is improving the resolution of the cryo-microscopy one step further to achieve cellular resolution. With that instrument we could which provides us with the utility to test the hypothesis that diabetes impacts the cell function of renal vascular and proximal tubule. Having cellular resolution will lead us to answer the following questions:

- Is renal endothelial cell function affected by disease?
- Is oxidative stress responsible for the changes observed in lung vascular cells during the disease?

Reference

[1] (January 2014). *Symposium Highlights Emerging Role of 3D Tissue Modeling in EHS*. Available: http://www.alttox.org/spotlight/056.html

[2] T. Vo-Dinh, *Biomedical photonics handbook*. Boca Raton, Fla.: CRC Press, 2003.

[3] B. Alberts, *Molecular biology of the cell*, 4th ed. New York: Garland Science, 2002.

[4] D. Voet, *et al.*, *Fundamentals of biochemistry : life at the molecular level*, 2nd ed. Hoboken, N.J.: Wiley, 2006.

[5] N. R. Pace, "The universal nature of biochemistry," *Proc Natl Acad Sci U S A*, vol. 98, pp. 805-8, Jan 30 2001.

[6] (March 2014). *Powerhouse Rules: The Role of Mitochondria in Human Diseases*. Available: http://ocw.mit.edu/courses/biology/7-342-powerhouse-rules-the-role-of-mitochondria-in-human-diseases-spring-2011/

[7] E. N. Marieb and K. Hoehn, *Human anatomy & physiology*, 8th ed. San Francisco: Benjamin Cummings, 2010.

[8] J. L. Spees, *et al.*, "Mitochondrial transfer between cells can rescue aerobic respiration," *Proc Natl Acad Sci U S A*, vol. 103, pp. 1283-8, Jan 31 2006.

[9] D. Voet, *et al.*, *Fundamentals of biochemistry : life at the molecular level*, 2nd ed ed. New York: Wiley, 2006.

[10] (January 2014). *The Electron Transport Chain Steps Simplified*. Available: http://www.dbriers.com/tutorials/2012/04/the-electron-transport-chain-simplified/

[11] H. Lodish, *Molecular cell biology*, 7th ed. New York, NY: W. H. Freeman and Co., 2012.

[12] T. M. Devlin, *Textbook of biochemistry : with clinical correlations*, 7th ed. Hoboken, NJ: John Wiley & Sons, 2011.

[13] N. Kango, *Textbook of Microbiology*. New Delhi: I.K. International Publishing House Pvt. Ltd., 2010.

[14] A. B. Fisher, "Intermediary metabolism of the lung," *Environ Health Perspect*, vol. 55, pp. 149-58, Apr 1984.

[15] J. M. Mates and F. M. Sanchez-Jimenez, "Role of reactive oxygen species in apoptosis: implications for cancer therapy," *Int J Biochem Cell Biol*, vol. 32, pp. 157-70, Feb 2000.

[16] W. L. Yen and D. J. Klionsky, "How to Live Long and Prosper: Autophagy, Mitochondria, and Aging," *Physiology*, vol. 23, pp. 248-262, Oct 2008.

[17] B. Halliwell and J. M. C. Gutteridge, *Free radicals in biology and medicine*, 4th ed. Oxford ; New York: Oxford University Press, 2007.

[18] T. M. Buttke and P. A. Sandstrom, "Oxidative Stress as a Mediator of Apoptosis," *Immunology Today*, vol. 15, pp. 7-10, Jan 1994.

[19] W. L. Yen and D. J. Klionsky, "How to live long and prosper: autophagy, mitochondria, and aging," *Physiology (Bethesda)*, vol. 23, pp. 248-62, Oct 2008.

[20] J. R. Lakowicz, *Principles of fluorescence spectroscopy*, 3rd ed. New York: Springer, 2006.

[21] S. L. Daugherty, *et al.*, "The association between medication adherence and treatment intensification with blood pressure control in resistant hypertension," *Hypertension*, vol. 60, pp. 303-9, Aug 2012.

[22] J. Ribas Gispert, *Coordination chemistry*. Weinheim: Wiley-VCH, 2008.

[23] (January 2014). *Excitation and Emission Fundamentals*. Available: http://www.olympusmicro.com/primer/techniques/fluorescence/excitation.html

[24] J. M. Christie, *et al.*, "LOV (light, oxygen, or voltage) domains of the blue-light photoreceptor phototropin (nph1): binding sites for the chromophore flavin mononucleotide," *Proc Natl Acad Sci U S A*, vol. 96, pp. 8779-83, Jul 20 1999.

[25] G. H. Patterson, *et al.*, "Separation of the glucose-stimulated cytoplasmic and mitochondrial NAD(P)H responses in pancreatic islet beta cells," *Proc Natl Acad Sci U S A*, vol. 97, pp. 5203-7, May 9 2000.

[26] B. Chance and H. Baltscheffsky, "Respiratory enzymes in oxidative phosphorylation. VII. Binding of intramitochondrial reduced pyridine nucleotide," *J Biol Chem*, vol. 233, pp. 736-9, Sep 1958.

[27] B. Chance, *et al.*, "Oxidation-reduction ratio studies of mitochondria in freeze-trapped samples. NADH and flavoprotein fluorescence signals," *J Biol Chem*, vol. 254, pp. 4764-71, Jun 10 1979.

[28] S. L. Bernard, *et al.*, "High spatial resolution measurements of organ blood flow in small laboratory animals," *Am J Physiol Heart Circ Physiol*, vol. 279, pp. H2043-52, Nov 2000.

[29] J. J. Kelly, *et al.*, "Regional blood flow measurements from fluorescent microsphere images using an Imaging CryoMicrotome," *Review of Scientific Instruments*, vol. 71, pp. 228-234, Jan 2000.

[30] (January 2014). *EXi Aqua Bio-Imaging Microscopy Camera*. Available: http://www.qimaging.com/products/cameras/scientific/exi_aqua.php

[31] (January 2014). *Rolera EM-C2™* Available: http://www.qimaging.com/products/cameras/scientific/rolera-emc2.php

[32] J. L. Prince and J. M. Links, *Medical imaging signals and systems*. Upper Saddle River, NJ: Pearson Prentice Hall, 2006.

[33] (February 2014). *LENS QUALITY: MTF, RESOLUTION & CONTRAST*. Available: http://www.cambridgeincolour.com/tutorials/lens-quality-mtf-resolution.htm

[34] (February 2014). *Optical resolution*. Available: http://en.wikipedia.org/wiki/Optical_resolution

[35] (February 2014). *Numerical Aperture and Resolution*. Available: http://micro.magnet.fsu.edu/primer/anatomy/numaperture.html

[36] (January 2014). *Optem Zoom 125C 12.5:1 Micro-Inspection Lens System*. Available: http://www.qioptiq.com/optem-micro-12-5.html

[37] J. W. Goodman, *Introduction to Fourier optics*, 3rd ed. Englewood, Colo.: Roberts & Co., 2005.

[38] (February 2014). *Optical aberration*. Available: http://en.wikipedia.org/wiki/Optical_aberration

[39] A. K. Ghatak, *Optics*. Boston: McGraw-Hill Higher Education, 2010.

[40] (February 2014). *What is Chromatic Aberration?* Available: http://photographylife.com/what-is-chromatic-aberration

[41] (February 2014). *Chromatic aberration*. Available: http://en.wikipedia.org/wiki/Chromatic_aberration

[42] (February 2014). *Magnification*. Available: http://personalsecurityzone.com/riflescope_school.htm

[43] A. H. Jobe and E. Bancalari, "Bronchopulmonary dysplasia," *American journal of respiratory and critical care medicine,* vol. 163, pp. 1723-9, Jun 2001.

[44] R. Sepehr, *et al.*, "Optical Imaging of Lipopolysaccharide-Induced Oxidative Stress in Acute Lung Injury from Hyperoxia and Sepsis," *Journal of Innovative Optical Health Sciences,* vol. 6, Jul 2013.

[45] S. Dias, *et al.*, "VEGF(165) promotes survival of leukemic cells by Hsp90-mediated induction of Bcl-2 expression and apoptosis inhibition," *Blood,* vol. 99, pp. 2532-2540, Apr 1 2002.

[46] S. Kondo, *et al.*, "Attenuation of retinal endothelial cell migration and capillary morphogenesis in the absence of Bcl-2," *American Journal of Physiology-Cell Physiology,* vol. 294, pp. C1521-C1530, Jun 2008.

[47] I. Georgakoudi, *et al.*, "NAD(P)H and collagen as in vivo quantitative fluorescent biomarkers of epithelial precancerous changes," *Cancer Research,* vol. 62, pp. 682-7, Feb 1 2002.

[48] N. Ramanujam, *et al.*, "In vivo diagnosis of cervical intraepithelial neoplasia using 337-nm-excited laser-induced fluorescence," *Proc Natl Acad Sci U S A,* vol. 91, pp. 10193-7, Oct 11 1994.

[49] B. Chance, *et al.*, "Intracellular oxidation-reduction states in vivo," *Science,* vol. 137, pp. 499-508, Aug 17 1962.

[50] L. K. Klaidman, *et al.*, "High-performance liquid chromatography analysis of oxidized and reduced pyridine dinucleotides in specific brain regions," *Anal Biochem,* vol. 228, pp. 312-7, Jul 1 1995.

[51] K. A. Mcallister, *et al.*, "Endoglin, a Tgf-Beta Binding-Protein of Endothelial-Cells, Is the Gene for Hereditary Hemorrhagic Telangiectasia Type-1," *Nature Genetics,* vol. 8, pp. 345-351, Dec 1994.

[52] A. Alt, *et al.*, "Structural and Functional Insights into Endoglin Ligand Recognition and Binding," *Plos One,* vol. 7, Feb 8 2012.

[53] H. M. Arthur, *et al.*, "Endoglin, an ancillary TGFbeta receptor, is required for extraembryonic angiogenesis and plays a key role in heart development," *Dev Biol,* vol. 217, pp. 42-53, Jan 1 2000.

[54] A. Bourdeau, *et al.*, "A murine model of hereditary hemorrhagic telangiectasia," *J Clin Invest,* vol. 104, pp. 1343-51, Nov 1999.

[55] D. Y. Li, *et al.*, "Defective angiogenesis in mice lacking Endoglin," *Science,* vol. 284, pp. 1534-7, May 28 1999.

[56] M. Mahmoud, *et al.*, "Pathogenesis of arteriovenous malformations in the absence of Endoglin," *Circ Res,* vol. 106, pp. 1425-33, Apr 30 2010.